Journal of Computational Physics **153,** 273–311 (1999)
Article ID jcph.1999.6268, available online at http://www.idealibrary.com on IDEAL®

On the Use of Shock-Capturing Schemes for Large-Eddy Simulation

Eric Garnier,* Michele Mossi,† Pierre Sagaut,* Pierre Comte,‡,* and Michel Deville†,*

*ONERA, 29, Avenue de la Division Leclerc, BP 72, 92322 Châtillon Cedex, France; †Laboratoire de Mécanique des Fluides, Ecole Polytechnique Fédérale de Lausanne, CH-1015 Lausanne, Switzerland; ‡IMG/LEGI, BP 53, 38041 Grenoble Cedex 9, France

E-mail:egarnier@onera.fr, michel.mossi@epfl.ch, sagaut@onera.fr, comte@hmg.inpg.fr, michel.deville@epfl.ch

Received February 16, 1998; revised March 18, 1999

Numerical simulations of freely decaying isotropic fluid turbulence were performed at various Mach numbers (from 0.2 to 1.0) using known shock-capturing Euler schemes (Jameson, TVD-MUSCL, ENO) often employed for aeronautical applications. The objective of these calculations was to evaluate the relevance of the use of such schemes in the large-eddy simulation (LES) context. The potential of the monotone integrated large-eddy simulation (MILES) approach was investigated by carrying out computations without viscous diffusion terms. Although some known physical trends were respected, it is found that the small scales of the simulated flow suffer from high numerical damping. In a quasi-incompressible case, this numerical dissipation is tentatively interpreted in terms of turbulent dissipation, yielding the evaluation of equivalent Taylor micro-scales. The Reynolds numbers based on these are found between 30 and 40, depending on the scheme and resolution (up to 128^3). The numerical dissipation is also interpreted in terms of subgrid-scale dissipation in a LES context, yielding equivalent Smagorinsky "constants" which do not level off with time and which remain larger than the commonly accepted values of the classical Smagorinsky constant. On the grounds of tests with either the Smagorinsky or a dynamic model, the addition of explicit subgrid-scale (SGS) models to shock-capturing Euler codes is not recommended.

Key Words: shock-capturing schemes; large-eddy simulation.

1. INTRODUCTION

At the present time, the need for unsteady fluid turbulent computations in the transonic flow regime is clearly identified for future aeronautical applications, and the improvement of computational resources opens the way to large-eddy simulation (LES). However, since in the transonic Mach number regime the use of shock-capturing schemes is inevitable, the influence of their intrinsic numerical dissipation on LES computations must be investigated.

0021-9991/99 $30.00

Such schemes will be considered as suitable for LES if they satisfy one of the following conditions:

- their numerical dissipation is much lower than the physical subgrid-scale dissipation (condition (C1))
- their numerical dissipation is able to mimic those of a subgrid-scale (SGS) model (condition (C2)).

These conditions correspond to the two approaches found in the literature. On the one hand, recently Ghosal [1] showed that the numerical errors of a centered scheme, even of eighth-order accuracy, can hide the contribution of a subgrid-scale model if a prefiltering technique is not applied. In the same way, Kravchenko and Moin [2] showed that, for turbulent channel flow, the truncation errors of second-order finite-difference simulations can exceed the magnitude of subgrid-scale terms. Moreover, for mixing-layer simulations with high-order compact schemes lacking shock-capturing properties, Vreman *et al.* [3] found it necessary to prefilter the resolved variables so that no energy is left at the mesh scale, in a consistent way with the conclusions of [1].

On the other hand, intrinsically dissipative discontinuity-capturing Euler schemes reproduce some trends of turbulence: let us mention the results of Kawamura and Kuwahara [4] in the incompressible regime and Porter *et al.* [5] in compressible cases. This approach is usually referred to as MILES (monotone integrated large-eddy simulation) and has been introduced by Boris *et al.* [6], who claimed that the intrinsic dissipation of the flux-corrected transport (FCT) algorithm can mimic the effects of a subgrid-scale model. Some authors, like Fureby *et al.* [7] in the incompressible regime, also include the viscous terms of the Navier–Stokes equations. In all cases, the relevance of this concept is not fully established, and the motivation of the present paper is to provide additional information to clarify this point and to check if one of the two conditions (C1) or (C2) is satisfied.

This paper is a follow-up of the work of Mossi [8], who challenged TVD-MUSCL and Jameson schemes to reproduce the incompressible Taylor–Green vortex-decay problem at finite Reynolds number, by comparisons with direct numerical simulations (DNS) of Brachet *et al.* [9]. In the present study, we moved to compressible isotropic turbulence at zero molecular viscosity, with a wider set of schemes, namely, the Jameson scheme, a TVD-MUSCL scheme using the minmod limiter with two different compression factors, and three schemes within the ENO family (ENO, WENO, MENO) (see Appendix A for a brief description of these).

The paper is organized as follows. In Section 2, the results obtained with these schemes at spatial resolutions 64^3 and 128^3 in five test cases at different initial rms Mach numbers ($M_{\text{rms}} = 0.2, 0.5$, and 1.0) and compressibility factors ($\chi_0 = 0$ and 0.05; see Section 2 for definition) are presented and compared. For the quasi-incompressible case ($M_{\text{rms}}, \chi_0) = (0.2, 0)$ the results are compared with spectral incompressible LES and DNS of Métais and Lesieur [10], Vincent and Meneguzzi [11], and She [12], so that equivalent Reynolds numbers based on the Taylor micro-scale can be worked out for each scheme and resolution. In Section 3, a more precise evaluation of the built-in dissipation of these schemes is proposed in terms of the "generalized Smagorinsky constant." The relevance of this concept is checked by repeating certain simulations with two different subgrid-scale models (the Smagorinsky and the dynamic eddy-viscosity models). The general conclusion is then given in Section 4.

2. THE MILES APPROACH

The Euler equations are solved in their conservative form

$$\frac{\partial \mathbf{U}}{\partial t} + \frac{\partial \mathbf{F}}{\partial x} + \frac{\partial \mathbf{G}}{\partial y} + \frac{\partial \mathbf{H}}{\partial z} = 0, \tag{1}$$

where t denotes time and (x, y, z) the 3D Cartesian coordinates. For an ideal gas of specific heat ratio γ ($\gamma = 1.4$ here, as in air), the state vector $\mathbf{U}$ and the convective fluxes $\mathbf{F}$, $\mathbf{G}$, and $\mathbf{H}$ are defined as

$$\mathbf{U} = \begin{pmatrix} \rho \\ \rho u \\ \rho v \\ \rho w \\ \rho \mathcal{E} \end{pmatrix}, \quad \mathbf{F} = \begin{pmatrix} \rho u \\ \rho u^2 + p \\ \rho uv \\ \rho uw \\ u(\rho \mathcal{E} + p) \end{pmatrix}, \quad \mathbf{G} = \begin{pmatrix} \rho v \\ \rho uv \\ \rho v^2 + p \\ \rho vw \\ v(\rho \mathcal{E} + p) \end{pmatrix}, \quad \mathbf{H} = \begin{pmatrix} \rho w \\ \rho uw \\ \rho vw \\ \rho w^2 + p \\ w(\rho \mathcal{E} + p) \end{pmatrix}, \tag{2}$$

where $(u, v, w) = \mathbf{u}$, ρ, p, and $\mathcal{E}$ are respectively the velocity vector, density, pressure, and total specific energy, $\mathcal{E} = p/(\rho(\gamma - 1)) + \frac{1}{2}\mathbf{u}^2$. All initial conditions are at uniform density ρ_0 and temperature T_0, that we use to make the problem non-dimensional, together with the rms of the initial random velocity field. Consequently, the initial rms Mach number (M_{rms}) arises naturally in the equation of state:

$$\frac{p}{\rho} = \frac{T}{\gamma M_{\text{rms}}^2}. \tag{3}$$

The time integration is performed with a Runge–Kutta multi-stage technique while the convective fluxes $\mathbf{F}$, $\mathbf{G}$, $\mathbf{H}$ are discretized with some widely used shock-capturing schemes, which are listed as follows and briefly presented in Appendix A:

- second-order accurate in space Jameson scheme using a four-stage Runge–Kutta time marching technique;
- third-order accurate in space TVD-MUSCL scheme with the minmod limiter and $\beta = 1$ (the minmod limiter and the compression factor β are defined in Appendix A.2) using a four-stage Runge–Kutta time marching technique, denoted MUSCL1;
- third-order accurate in space TVD-MUSCL scheme with the minmod limiter and $\beta = 4$ using a four-stage Runge–Kutta time marching technique, denoted MUSCL4;
- third-order accurate in space ENO scheme using a three-stage Runge–Kutta TVD time marching technique [13];
- fourth-order accurate in space WENO scheme using a three-stage Runge–Kutta TVD time marching technique;
- fifth-order accurate in space MENO scheme using a three-stage Runge–Kutta TVD time marching technique.

Each order of accuracy mentioned above corresponds to the maximal order that each scheme is able to reach in the smooth regions of the flow. Among these six numerical schemes, the Jameson scheme is the only one which allows direct control of the numerical dissipation by means of an artificial dissipation model. Here, the scalar dissipation model proposed by Jameson *et al.* [33] has been employed. The two coefficients controlling the artificial dissipation $\kappa^{(2)}$ and $\kappa^{(4)}$ (see Eq. (21)) can be chosen as a function of the spatial configuration and

TABLE I
Key Parameters of the Different Cases

	Case 1	Case 2	Case 3	Case 4	Case 5
Initial rms Mach number	0.2	0.5	0.5	1.0	1.0
Initial compressibility ratio χ_0	0	0	0.05	0	0.05

of the physical problem. Actually, for industrial computations, the former varies typically between 1.0 and 2.0, while the second is in the range of 0.01 and 0.05. In all simulations presented here, $\kappa^{(2)}$ and $\kappa^{(4)}$ were set to 1.0 and 0.03, respectively. This choice is surely neither the least dissipative one nor the best for the problem at hand, but it is widely used for industrial flow calculations. A detailed analysis of the influence of $\kappa^{(2)}$ and $\kappa^{(4)}$ with several artificial dissipation models can be found in [8].

All simulations are performed in a cube of edge length 2π, containing either 64^3 or 128^3 uniformly distributed grid points. The boundary conditions are periodic in the three directions. Helmholtz decomposition of the velocity vector can be performed efficiently in the spectral space. The compressible part of the velocity $\mathbf{u_k}$ is defined and computed as $\mathbf{u}^c_\mathbf{k} = [\mathbf{k}\cdot\mathbf{u_k}]\mathbf{k}/k^2$, and the solenoidal part as $\mathbf{u}^s_\mathbf{k} = \mathbf{u_k} - \mathbf{u}^c_\mathbf{k}$. The corresponding spectra are

$$E(k) = \frac{1}{2}\sum_{k-1/2<|\mathbf{k}|\le k+1/2} |\mathbf{u_k}|^2; \qquad E_c(k) = \frac{1}{2}\sum_{k-1/2<|\mathbf{k}|\le k+1/2} \left|\mathbf{u}^c_\mathbf{k}\right|^2, \tag{4}$$

and their corresponding energies are

$$\mathbf{E} = \int_0^\infty E(k)\,dk; \qquad \mathbf{E}_c = \int_0^\infty E_c(k)\,dk. \tag{5}$$

The compressibility ratio χ is then defined as $\chi = \mathbf{E}_c/\mathbf{E}$. Its initial value χ_0 is of importance, as stressed in particular by Passot and Pouquet [14], Blaisdell *et al.* [15], and Erlebacher *et al.* [16].

In all the cases considered here, which are summarized in Table I, the initial velocity fields have power-law spectra $\sim k^4 e^{-2(k^2/k_0^2)}$ with $k_0 = 2$. All simulations have been carried out up to $t = 10$, which corresponds to $10/\pi \approx 3$ initial eddy-turnover times.

2.1. *The Shock-Free Almost Incompressible Case*

Case 1 does not develop strong compressibility effects (for all schemes, χ remains less than 0.01). It is therefore relevant to compare our results with the numerous studies of freely decaying incompressible isotropic turbulence computations, in addition to the low-Mach-number results of Erlebacher *et al.* [16]. Because the effective filter (both transfer function and cut-off length scale) associated to MILES calculations remains unknown, results will be compared directly with unfiltered DNS results.

The first aspect to be checked is the ability of the dissipative Euler schemes under investigation to recover proper Navier–Stokes dynamics (instead of the equipartition-type solutions produced by certain academic and even industrial codes). As explained in the monograph by Lesieur [17], the evolution at large (but finite) Reynolds numbers of freely decaying incompressible isotropic turbulence decay follows essentially two distinct stages. During the

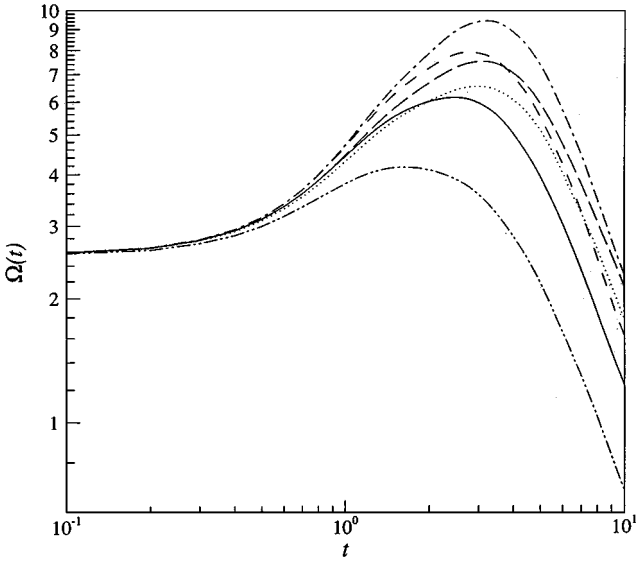

FIG. 1. Time history of enstrophy for test Case 1 (64^3 grid). ENO ———; WENO -----; MENO -·-·-·-; Jameson · · ·; MUSCL4 – – – – –; MUSCL1 -·-·-·.

first stage, the viscous effects are negligible, the flow develops strongly anisotropic events (sheets rolling-up into worm-like vortices), and enstrophy increases dramatically due to vortex stretching. During the second stage, viscous diffusion plays an important role in the dynamics and distorted dissipative structures are created; moreover, the enstrophy

$$\Omega = \frac{1}{2}\langle \omega^2 \rangle = \frac{1}{2}\langle |\nabla \times \mathbf{u}|^2 \rangle \tag{6}$$

reaches a maximum and decays. All statistics then become self-similar. In Eq. (6), the brackets $\langle \cdot \rangle$ denote the statistical average on all mesh points.

The two stages can be recognized in Figs. 1 and 2, which show the time evolution of enstrophy for the 64^3 grid and the 128^3 grid, respectively. From $t = 0$ to about 3, enstrophy grows and small structures are generated; then, the numerical damping, which becomes strong for small scales, leads to a decrease of enstrophy. Comparing these figures with the one sketched by Lesieur [17, Fig. VI-5, p. 153], one could note that the global evolution of the enstrophy is in agreement with the EDQNM (eddy-damped quasi-normal Markovian approximation) predictions, which has also been confirmed by the previous tests on the Taylor–Green problem [8]. The enstrophy level increases with the resolution in the same way as it would increase with the Reynolds number in Navier–Stokes computations (up to scaling exponents that will be considered later).

The EDQNM theory predicts that, at zero molecular viscosity, enstrophy blow-up occurs at the critical time $t_c \sim 5.9/\Omega(0)^{1/2}$. At finite Reynolds number, enstrophy no longer blows up, but exhibits a peak about t_c, that would correspond to $t = 3.7$ here. More precisely, DNS results (see in particular Ref. [9] with Taylor–Green initial conditions) show that the peak time decreases continuously when molecular viscosity increases, which can be used as an indirect measure of an equivalent Reynolds number in our case. We are of course aware of the fact that such equivalent Reynolds numbers are resolution dependent.

Figures 1 and 2 show that the peak time ranges from 2.5 for the MUSCL1 scheme with the 64^3 grid to 4.0 for the MENO scheme with the 128^3 grid. On the coarse grid, the enstrophy

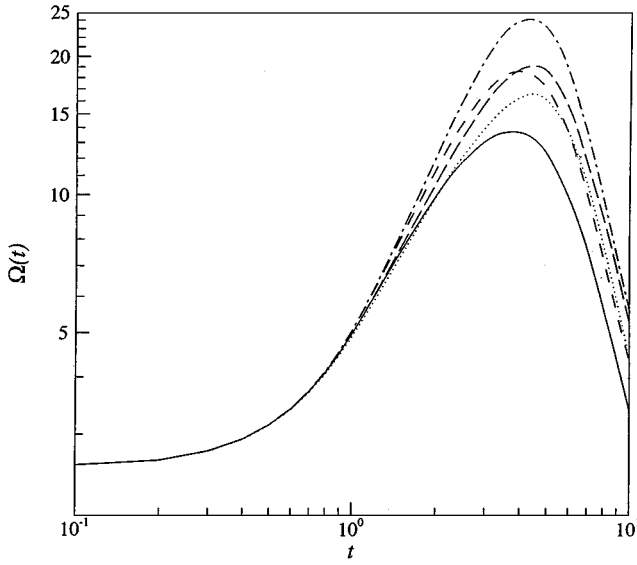

FIG. 2. Time history of enstrophy for test Case 1 (128^3 grid). ENO ———; WENO -----; MENO -·-·-·-·-; Jameson · · ·; MUSCL4 – – – – –.

of the MUSCL4 scheme begins to be larger than the one of the WENO scheme soon after the enstrophy peak. This suggests that the WENO scheme is more diffusive at small scales than the MUSCL4 one; whereas, when the spectrum is not completely filled, the WENO scheme is less diffusive than the MUSCL4 one. Since the differences between the schemes begin to be noticeable after $t = 1$, i.e., well before t_c, we suspect that numerical dissipation affects not only the small scales but also the large ones. The MENO scheme preserves the largest amount of enstrophy until the end of the simulation. This suggests that it is the least dissipative of all, which will be confirmed further on. After the MENO scheme, the order in terms of increasing dissipation is as follows: WENO, MUSCL4, Jameson, ENO, and MUSCL1. The latter scheme was found too dissipative at 64^3 to justify further testing (see Fig. 1). It was checked that the use of the smoothness indicator of the WENO scheme given in [18] produces the same results with a 3% relative error on enstrophy with respect to the one of [19] used in this study.

The time history of the total kinetic energy, presented in Figs. 3 and 4 for both grids, shows that numerical diffusion acts earlier than the above enstrophy peak time, more visibly on the coarse grid, of course. At $t = 10$, the rank between the schemes is identical for both grids. The Jameson scheme preserves the largest amount of energy, followed by the MUSCL4, MENO, WENO, ENO, and MUSCL1 schemes. For the latter, the energy begins its decay sooner than the others, which is, again, evidence that the large scales of the flow suffer from numerical diffusion. The time history of the energy decay shows that, until at least $t = 3$, the MENO scheme contains more energy than the other schemes. The kinetic energy is found to decrease as $t^{-\alpha}$ with α ranging from 1.3 (MUSCL1) to 1.67 (MUSCL4) on the coarse grid and from 1.94 (ENO) to 2.18 (MUSCL4) on the fine grid. For the latter grid, decay rates are greater than the values of 1.38 predicted by EDQNM and of 1.6 found in spectral DNS [10]. Note that a ENO scheme on a 32^3 grid gives a slope of 1.2. Here, the trend is an increase of α when increasing the resolution. An explanation for this behavior is that the wave number range to dissipate energy is broader in the 128^3 computation than

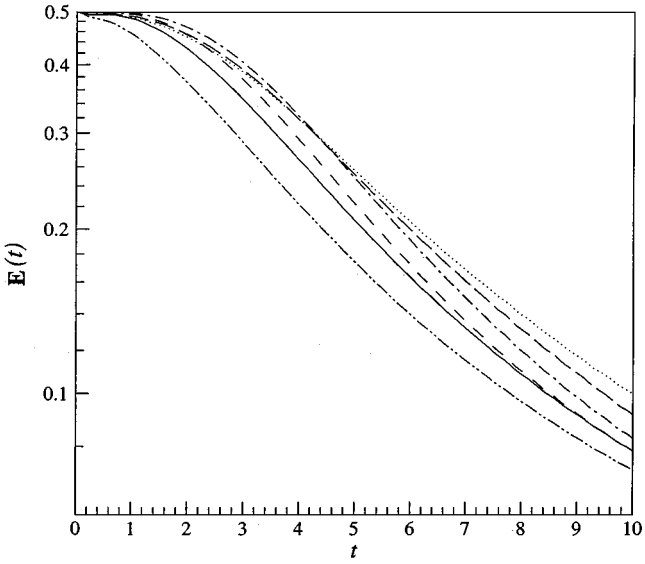

FIG. 3. Time history of energy decay for test Case 1 (64^3 grid). ENO ———; WENO -----; MENO -·-·-·-·-; Jameson · · ·; MUSCL4 – – – – –; MUSCL1 -·-·-·-.

in 64^3 computations (this assumption will be discussed later on with the help of other statistics).

Another test of validity of the MILES approach is the analysis of the schemes ability to produce $k^{-5/3}$ spectral sub-ranges in the self-similar decay stage. Looking at the kinetic energy spectrum of Fig. 5 for the 64^3 grid a $t = 10$, no such sub-ranges are clearly distinguishable. We will see in Section 3 that clearer $k^{-5/3}$ sub-ranges are obtained at the

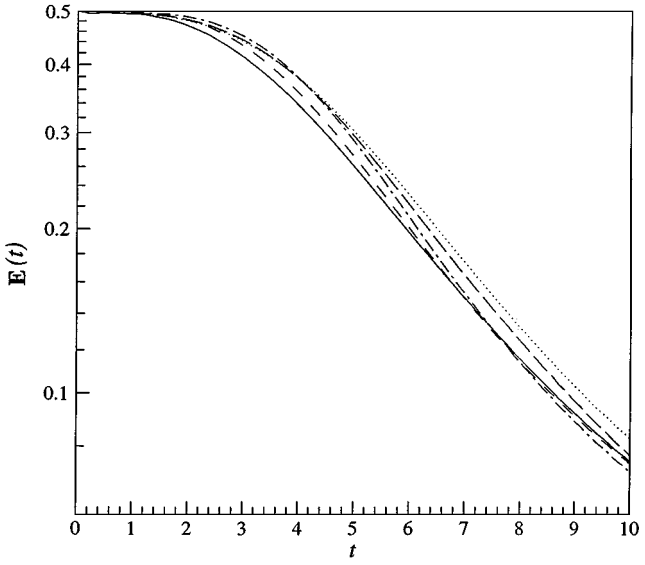

FIG. 4. Time history of energy decay for test Case 1 (128^3 grid). ENO ———; WENO -----; MENO -·-·-·-·-; Jameson · · ·; MUSCL4 – – – – –.

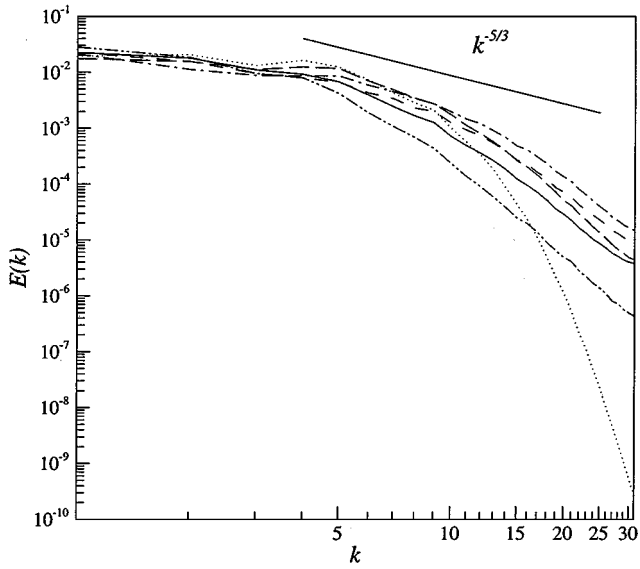

FIG. 5. Kinetic energy spectrum for test Case 1 at $t = 10$ (64^3 grid). ENO ———; WENO -----; MENO -·-·-·-·-; Jameson · · ·; MUSCL4 – – – – –; MUSCL1 ·····.

same resolution with a fourth-order Euler centered scheme coupled to a Smagorinsky SGS model.

A quite surprising behaviour is observed for the Jameson scheme, which does not leave any energy at the cut-off wave number ($k_c = N/2$, with $N = 64$ or 128): for both grids (see Figs. 5 and 6), the spectra obtained with this scheme resemble more low-Reynolds-number DNS spectra (with a Kolmogorov wavenumber $k_d \approx 18$ at 128^3) than high-Reynolds-number LES spectra. This behaviour depends on the artificial dissipation: indeed, with the less often

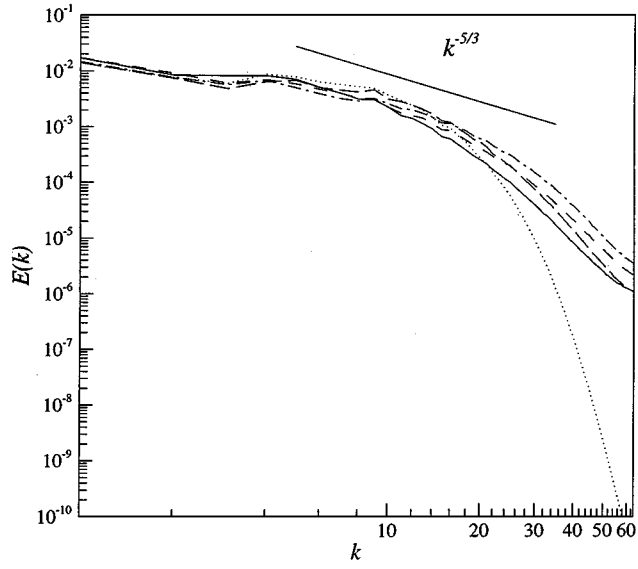

FIG. 6. Kinetic energy spectrum for test Case 1 at $t = 10$ (128^3 grid). ENO ———; WENO -----; MENO -·-·-·-·-; Jameson · · ·; MUSCL4 – – – – –.

used Jameson coefficients $\kappa^{(2)} = 1.0$ and $\kappa^{(4)} = 0.01$, results close to MUSCL4 ones are obtained, while even better results can be produced with matrix artificial dissipation models (see [8]). Nevertheless, the Jameson scheme better preserves energy in the large scales. This is quite understandable if one accepts the above analogy: in this case, the pseudo dissipative range about k_d would inhibit all transfers across k_c, yielding less energy dissipation in the large scales than with the other schemes. As a result, the total kinetic energy (the integral of the spectrum) is larger with the Jameson scheme than with the other ones, as stated above. On the 128^3 grid (see Fig. 6), all the other schemes exhibit a very short $k^{-5/3}$ sub-range, between the wave numbers 5 and 15. But, transfers should be examined in order to prove that inertial behaviour can be reproduced with the MILES approach. Whatever the conclusion of such investigation, the condition (C2) is not verified since classical LES is able to produce an inertial range up to the cut-off. Concerning the numerical scheme, one can notice that the MENO scheme yields more energy than the other ones at high wave numbers.

In DNS, the isotropic Taylor micro-scale λ (see Figs. 7 and 8), defined as in Jiménez *et al.* [20] by

$$\lambda^2 = \frac{5 \int_0^\infty E(k)\, dk}{\int_0^\infty k^2 E(k)\, dk} = \frac{5\mathbf{E}}{\Omega}, \tag{7}$$

is consistent with the classical definition of λ (see, e.g., Hinze [21]), which is one-dimensional and, in some sense, characteristic of the velocity gradients in the inertial range, when there is one. In Porter *et al.* [5], the same formula (up to the factor 5) was used as a measure of the resolved gradients in shock-capturing Euler simulation in the same spirit as the present ones, although one might object that the certainly crucial contribution of the subgrid-scales is not taken into account in this case. Note that the same problem arises in any LES, where the use of Eq. (7) has nevertheless become customary. As in the MILES results of Porter *et al.* [22, 5] and the LES/DNS simulations of Erlebacher *et al.* [16], λ keeps on increasing at large times,

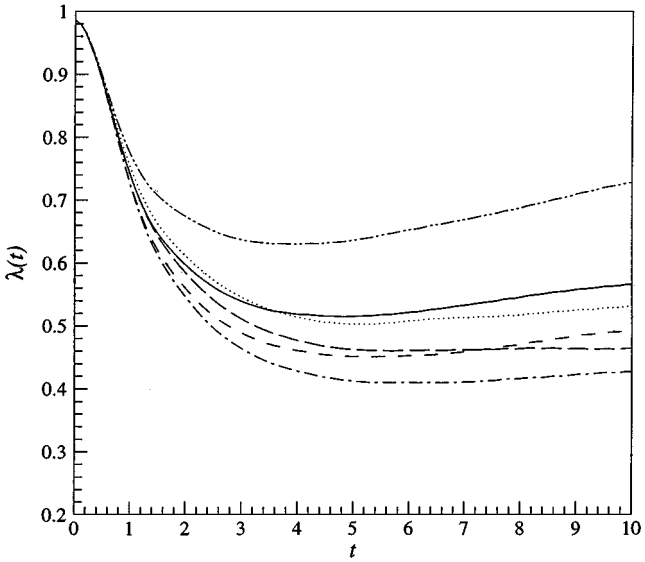

FIG. 7. Time history of Taylor micro-scale for Case 1 (64^3 grid). ENO ———; WENO -----; MENO -·-·-·-; Jameson · · ·; MUSCL4 – – – – –; MUSCL1 -·-·-·-.

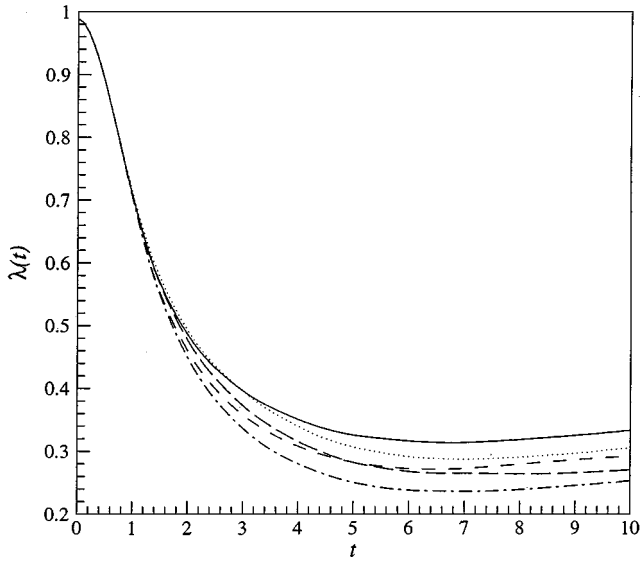

FIG. 8. Time history of Taylor micro-scale for Case 1 (128^3 grid). ENO ———; WENO -----; MENO -·-·-·-·-; Jameson · · ·; MUSCL4 – – – – –.

which is the expected behaviour. Furthermore, when the mesh size is reduced by half, λ is divided by a factor of about 1.6 for all the schemes, suggesting that it scales in $N^{-2/3}$ as expected from Kolmogorov's law. The main goal of this paper being the comparative assessment of the different schemes, the respective values of λ at $t = 10$ are summarized in Table II for both grids. On these grounds, MENO provides better results than MUSCL4, WENO, Jameson, ENO, and MUSCL1. Note that the Taylor micro-scale increases with the resolution. Moreover a 32^3 computation with an ENO scheme gives a value of 4 Δ for the Taylor micro-scale. This confirms that a higher resolution allows the numerical schemes to dissipate on a broader wave number range. Although this result seems to be counter-intuitive with respect to truncation analysis, it should be stressed that the finest grid used in our numerical computations is still far from the situation where the asymptotic behaviour for mesh size going to zero is expected.

Another way to investigate how realistic these inviscid simulations are is to look at the resolved skewness tensor

$$Sk_{ij} = \left\langle \left(\frac{\partial u_i}{\partial x_j} \right)^3 \right\rangle \Bigg/ \left\langle \left(\frac{\partial u_i}{\partial x_j} \right)^2 \right\rangle^{\frac{3}{2}}, \qquad 1 \le i, j \le 3, \tag{8}$$

where i and j refer to the $\mathbb{R}^3$ directions, as will be the case in the sequel of this paper.

TABLE II
Pseudo Taylor Micro-scale Values for All Schemes and Both Grids (Case 1, $t = 10$, $\Delta = 2\pi/N$)

	ENO	WENO	MENO	Jameson	MUSCL4	MUSCL1
64^3	5.8 Δ	5.0 Δ	4.3 Δ	5.4 Δ	4.7 Δ	7.4 Δ
128^3	6.8 Δ	5.9 Δ	5.1 Δ	6.2 Δ	5.5 Δ	

TABLE III
The Average of the Diagonal Components of the Resolved Skewness Tensor at $t = 10$ for Case 1

	ENO	WENO	MENO	Jameson	MUSCL4
64^3	−0.32	−0.32	−0.33	−0.45	−0.36
128^3	−0.37	−0.36	−0.35	−0.46	−0.34

The typical values for the diagonal components of the "true" skewness tensor reach -0.4 in experimental grid turbulence [23] and -0.5 in the incompressible DNS of Vincent and Meneguzzi [11], which agrees with the 96^3 grid points compressible DNS of Erlebacher *et al.* [16]. Initially, the skewness is close to zero, due to the Gaussian (random) initialization. A minimal requirement for the MILES approach would be a resolved skewness which becomes and remains negative. The averages of the diagonal components $1/3\ \mathrm{Tr}(Sk)$ are given in Table III at $t = 10$ for the two grids. All the schemes tested are able to develop a non-Gaussian behaviour but the values are relatively far from the aforementioned spectral or experimental calculations. These schemes introduce more numerical errors than the spectral ones usually used in theoretical turbulence studies. The results are close to the value of -0.3 found by Vreman *et al.* [24] in 21^3 LES computations of decaying isotropic turbulence at $M_{\mathrm{rms}} = 0.05$. Inspecting Table III one may notice that, except for the MUSCL4 scheme, the absolute value of the diagonal part of the skewness tensor increases with the resolution. The Jameson scheme is closer to the accepted value of -0.5 than the other ones, which confirms that its behaviour (with the standard set of coefficients) is closer to a low-Reynolds-number DNS than a high-Reynolds number LES.

Another minimal requirement for the schemes investigated here is to reproduce the basic mechanisms of turbulence like vortex stretching and the subsequent vortex tubes called "worms," discovered numerically by She (see in particular Ref. [12]; the discovery of the sheets from which they result is due to [11]). Figures 9 and 10 show iso-surfaces of constant vorticity magnitude at $t = 10$ for all the schemes on the 128^3 and 64^3 grids, respectively. The value of the iso-surfaces is chosen to be a proportion of the rms vorticity $\langle\omega^2\rangle^{1/2}$. For the 128^3 grid, the threshold value $\breve{\omega}$ is fixed so that $\breve{\omega} = 2.27\langle\omega^2\rangle^{1/2}$, while for the 64^3 grid $\breve{\omega}$ is only $2\langle\omega^2\rangle^{1/2}$. It is remarkable that for all schemes this choice produces the best visual impression, i.e., a compromise between the largest number of worms and the sharpness of the visualizations. These schemes are seen to produce elongated vorticity structures as found in spectral DNS simulations. The worm diameter is a direct function of the resolution and is about $5\ \Delta$ for the Jameson scheme and $3\ \Delta$ for the others.

Quantitative comparisons at $t = 10$ are shown in Fig. 11, where the probability density functions (pdfs) of velocity derivatives and pressure are plotted. Our data are compared with the data obtained by the incompressible DNS spectral computations by Métais and Lesieur [10], Vincent and Meneguzzi [11], and She [12]. The pdfs of $\partial u/\partial x$ and $\partial u/\partial y$ exhibit a non-Gaussian behaviour as expected from the results of the aforementioned authors. Our results are closest to those of Métais and Lesieur at $Re_\lambda \approx 20$ and of She at $Re_\lambda \approx 24$. In contrast, the pdfs of Vincent and Meneguzzi at $Re_\lambda \approx 150$ show larger tails than those provided by the shock-capturing schemes.

Since in incompressible flows, the low pressure levels are well correlated with intense vorticity, the pressure pdfs are strongly skewed toward the low values, as shown by Métais

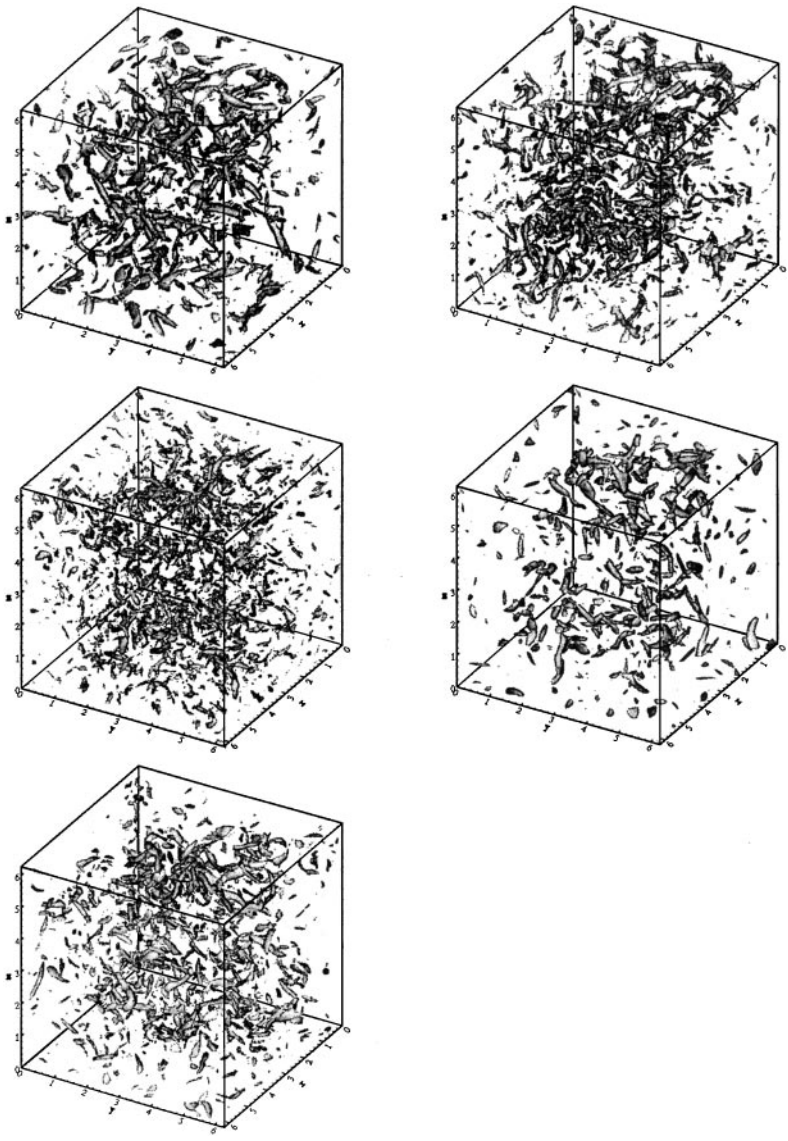

FIG. 9. Iso-surfaces of constant vorticity magnitude at $t = 10$ for all schemes in the 128^3 grid, Case 1. ENO, top left; WENO, top right; MENO, middle left; Jameson, middle right; MUSCL4, bottom left.

and Lesieur [10], who found exponential distributions for the negative pressure fluctuations. Looking at Fig. 11, one can observe that the shock-capturing schemes tested here are unable to reproduce the exponential "wings," and rather exhibit a Gaussian behaviour. A visualization of low pressure field of the WENO scheme on the 128^3 grid (the other schemes have the same behaviour) shows that pressure evolution is decorrelated from that of the vortices (See Fig. 12). This conclusion was checked to be independent of the selected pressure level. It may be added that the velocity pdfs have been found to be very closely Gaussian for all schemes, as expected (see, e.g., [10]).

The general conclusion of this section is that the condition (C2) is not satisfied since the statistics dependent on the small scales are very much influenced by the numerical damping.

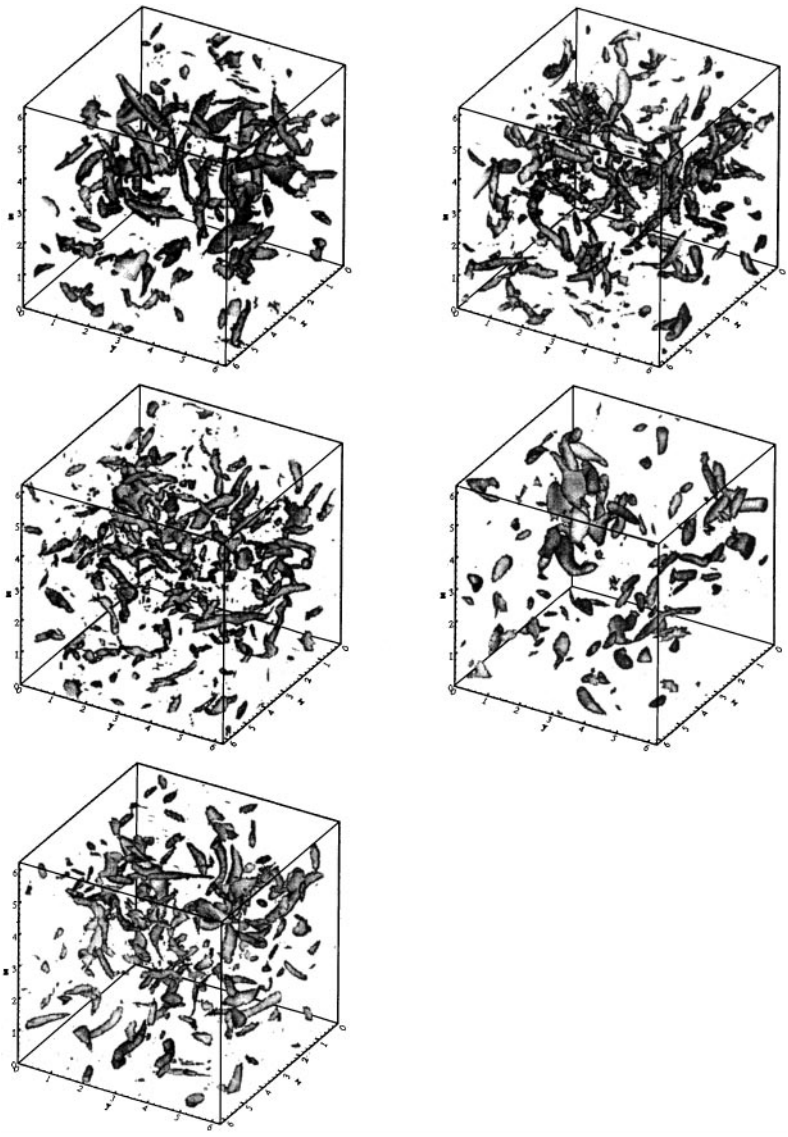

FIG. 10. Iso-surfaces of constant vorticity magnitude at $t = 10$ for all schemes in the 64^3 grid, Case 1. ENO, top left; WENO, top right; MENO, middle left; Jameson, middle right; MUSCL4, bottom left.

Moreover, the pdfs of the velocity derivatives exhibit a behaviour similar to a low Reynolds number DNS whereas the goal of the MILES approach is to emulate a LES result. Moreover, the pressure pdfs are seen to be essentially Gaussian.

Nevertheless, some global features of the turbulence are recovered and if one only needs a good representation of the large scales behaviour of the flow in turbulent applications, computations with the ENO, WENO, MUSCL4, and MENO schemes may be considered. The Jameson scheme exhibits very strong numerical damping at small scales with the set of artificial dissipation coefficients commonly used for transonic industrial applications. However, it was found that for lower coefficients the small scale behaviour was similar to that of the other schemes.

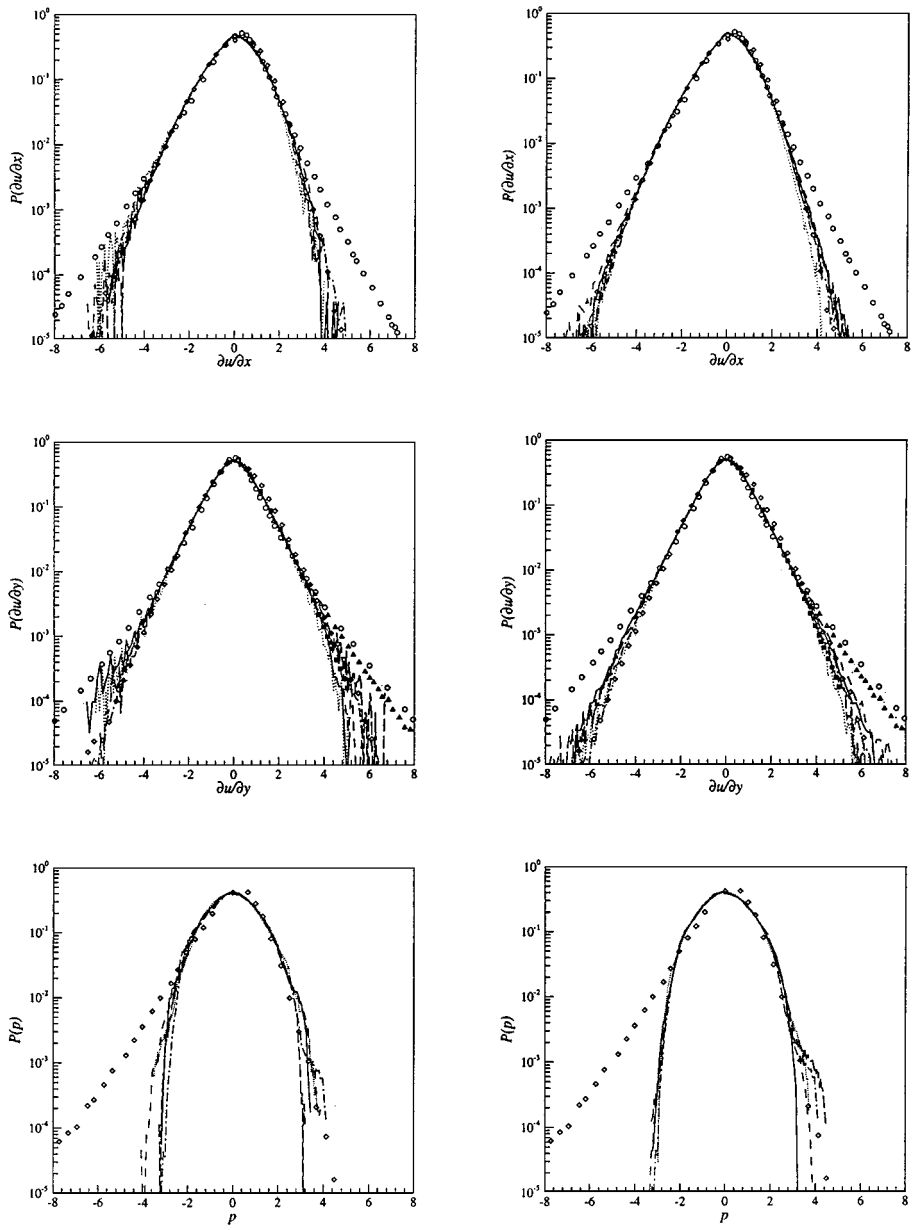

FIG. 11. Probability density functions $P(X)$ at $t = 10$ for Case 1. $X = \partial u/\partial x - 64^3$, top left; $X = \partial u/\partial x - 128^3$, top right; $X = \partial u/\partial y - 64^3$, middle left; $X = \partial u/\partial y - 128^3$, middle right; $X =$ pressure $- 64^3$, bottom left; $X =$ pressure $- 128^3$, bottom right. ENO ———; WENO - - - -; MENO - · - · - ·; Jameson · · ·; MUSCL4 – – – – –. Métais and Lesieur [10] ($Re_\lambda \approx 20$) ◇; She [12] ($Re_\lambda \approx 24$) ■; She [12] ($Re_\lambda \approx 77$) △; Vincent and Meneguzzi [11] ($Re_\lambda \approx 150$) ○.

The compression factor in the minmod limiter of the MUSCL scheme should be tuned to 4 to reduce numerical dissipation. This provides better results with more energy in all the wave lengths. The robustness of the MUSCL4 scheme is sufficient for all the cases tested in this study.

The quasi-equivalence between the results obtained by MUSCL4, WENO, or MENO, despite their different formal order of spatial accuracy, suggests that the use of a large moving

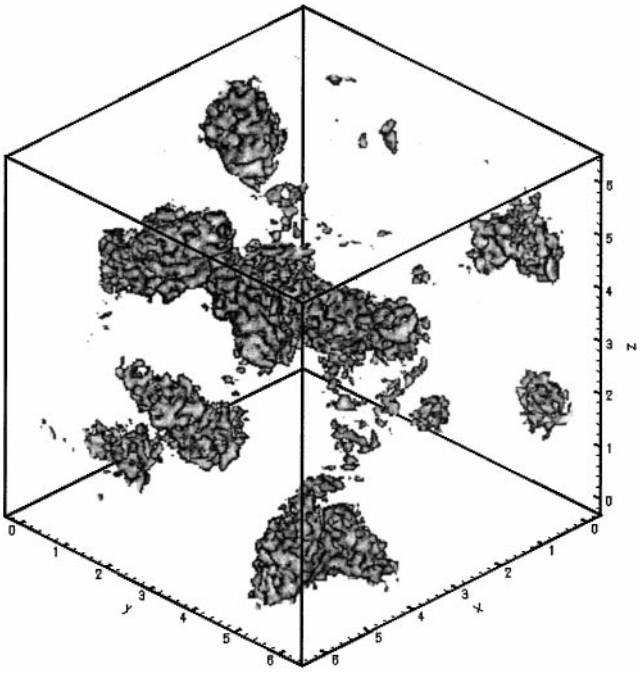

FIG. 12. Iso-surfaces of pressure for the WENO scheme at $t = 10$ (Case 1, 128^3 grid).

stencil in ENO schemes is not optimal for the simulation of highly turbulent flows. Looking at the small scale dissipation of these schemes, one can legitimately ask the question of the relative influence of the numerical dissipation with respect to a subgrid-scale model and one may suspect that the condition (C1) is not respected too.

2.2. *The Sonic Compressible Case*

Case 5 (see Table I) is close to the one simulated with the piecewise parabolic method (PPM) Euler scheme by Porter *et al.* [5]. In their MILES calculations, performed with $M_{\text{rms}} = 1.0$ and $\chi_0 = 0.068$ at high resolution (512^3 grid points), they distinguished three temporal phases: the "onset phase," with the formation of shocks at its end, ranging from $t = 0$ to 0.95 (the results of Porter *et al.* are given in our time units multiplying by π their time scale); the supersonic phase with the development of strong density contrasts ($\rho_{\max}/\rho_{\min}$) with $0.95 < t \leq 6.6$; and a post-supersonic phase dominated by vortex interaction and vortical decay for $t > 6.6$. These phases can be recognized in Fig. 13, where the time evolution of the density contrast is plotted for the MUSCL4 scheme on the finer mesh (the other schemes have the same behaviour).

The first phase spreads over the time interval $0 < t < 1.0$; the second, including shocks interaction, expands in the time interval $1.0 < t < 7.3$; and the last, where the density contrast mean slope is low, occurs for $t > 7.3$. These values are close to those found by Porter *et al.* and the physical trends are reproduced.

The time history of the energy decay is presented in Fig. 14 for the schemes considered here on the 128^3 grid and for the PPM computation of Porter *et al.* During the first phase ($t < 1$), there is close agreement between the different schemes. In the second phase, the

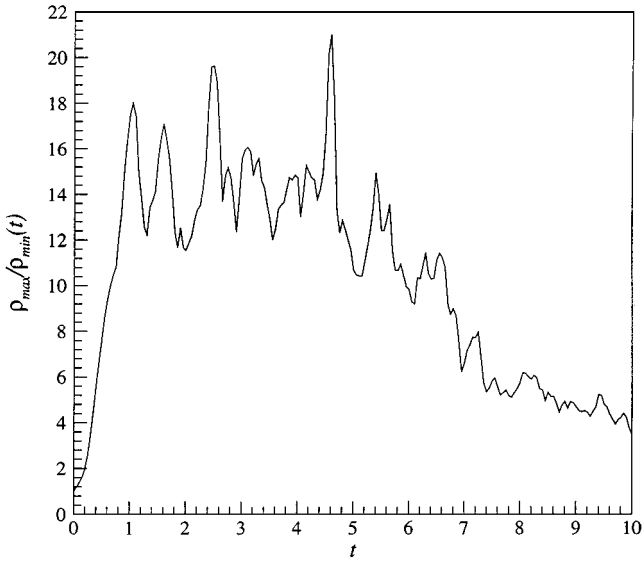

FIG. 13. Time history of density contrast for the MUSCL4 scheme (Case 5, 128^3 grid).

PPM scheme preserves more energy than the other schemes, but during the third phase the energy level is equivalent and the decay rates are very close.

Porter *et al.* explain that the time for compressional modes to develop fully is considerably shorter than the time for solenoidal modes to develop through the energy cascade. The spectrum of compressional energy is saturated at $t = 1$ when the shocks start to form. The time for solenoidal modes to develop is slower because it is linked with the eddy rotation time of the energy containing scales. Looking at Fig. 15, which shows the solenoidal and the

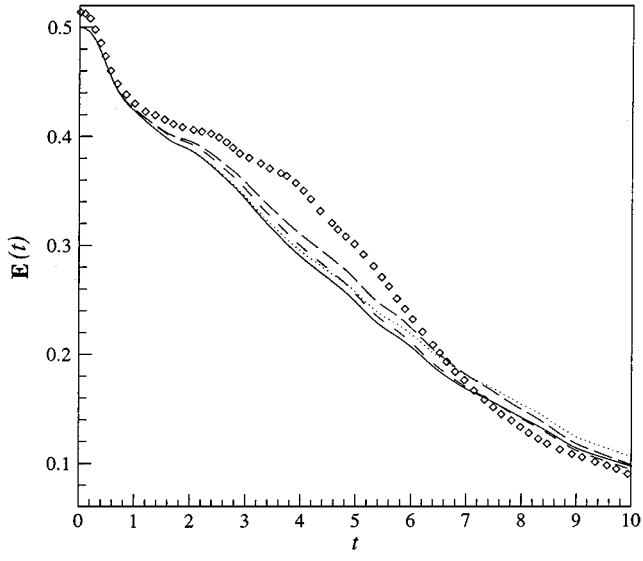

FIG. 14. Time history of energy decay for the tested schemes compared with the PPM scheme of Porter *et al.* (Case 5, 128^3 grid). ENO ———; WENO -----; PPM ◇; Jameson · · ·; MUSCL4 – – – – –.

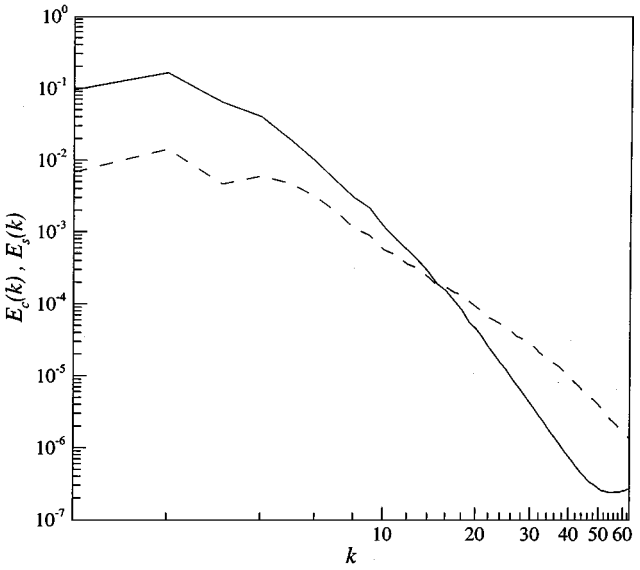

FIG. 15. Comparison between compressible $E_c(k)$ ----- and solenoidal $E_s(k)$ ——— kinetic energy spectra at $t = 1$ (Case 5, MUSCL4 scheme on 128^3 grid).

compressible spectra at $t = 1$ for the MUSCL4 scheme on the 128^3 grid, one can observe, as these authors did, that the compressible modes contain more energy than the solenoidal ones for high wave numbers (here for $k > 15$).

During the supersonic phase, compressional modes establish a k^{-2} velocity power spectrum as mentioned by Porter *et al.* The kinetic energy spectra at time $t = 5$ are given in Fig. 16 on the 128^3 mesh. All the simulations establish a k^{-2} slope between the modes 5 and 15. The first scheme which diverges from the k^{-2} slope is the ENO one.

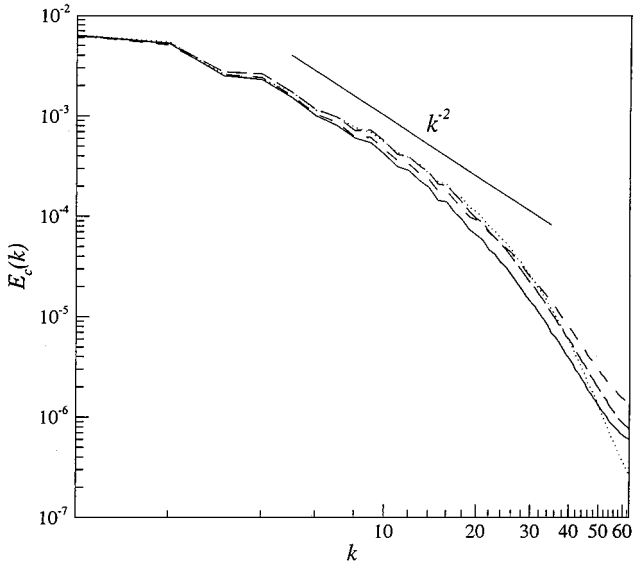

FIG. 16. Compressible kinetic energy spectrum at $t = 5$ for Case 5, a k^{-2} slope is also represented (128^3 grid). ENO ———; WENO -----; Jameson · · ·; MUSCL4 – – – – –.

Finally, it was observed that some of the computations became unstable on the finest mesh. This concerned the WENO scheme for test Case 4 and the MENO scheme for test Cases 4 and 5. In these cases, the local Mach number became as high as 3. Moreover, these schemes were likely to encounter difficulties in selecting a smooth stencil, probably when some strong gradients are present on all the possible stencils.

2.3. *Influence of the Mach Number and of the Compressibility*

The time evolution of the parameter χ for the five test cases is plotted in Fig. 17 for the ENO scheme on the finest mesh. Cases 3, 4, and 5 possess about 10% of compressible energy at $t = 10$. One can observe that, despite the incompressible initialization of Case 4, the value of χ is of the same order as for Case 5 just after 0.4 time units. For the shock-free case, χ is lower than 0.01 but, as in Case 2, this value seems to increase. Zang *et al.* [25] have mentioned that χ slightly increases when χ_0 is less than 0.5.

In Fig. 18, which shows the time history of the rms density ρ_{rms} for the five test cases, the density fluctuations are directly correlated with the initial Mach number as was also shown in [25]: the rms density increases with the Mach number. Comparing the initially incompressible cases with the ones containing compressible modes, one can notice that a non-zero value of χ_0 involves a higher value of ρ_{rms} than the one obtained with $\chi_0 = 0$. It is shown in Fig. 19 that the density contrast can be higher in Case 4 than in Case 5. It may be more physical to initialize the flow with a non-zero value of χ_0 when the rms Mach number is set to 1. However, this observation is not valid for Cases 2 and 3.

For the next comparison, the result of Case 5 could be easily extended to Case 4. As expected, the results of the $M_{\text{rms}} = 0.5$ cases stand between Cases 1 and 5 though the dynamics of these flows seem to be mostly incompressible.

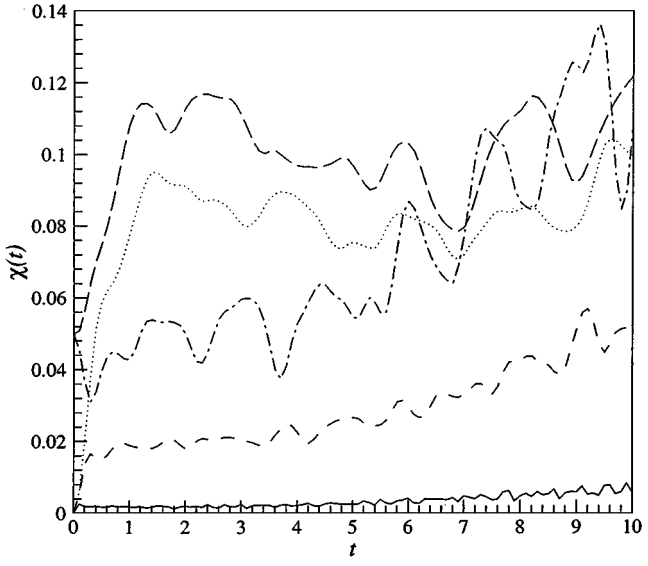

FIG. 17. Time history of χ for the ENO scheme (128^3 grid). Case 1 ———; Case 2 -----; Case 3 -·-·-·-·-; Case 4 · · ·; Case 5 – – – – –.

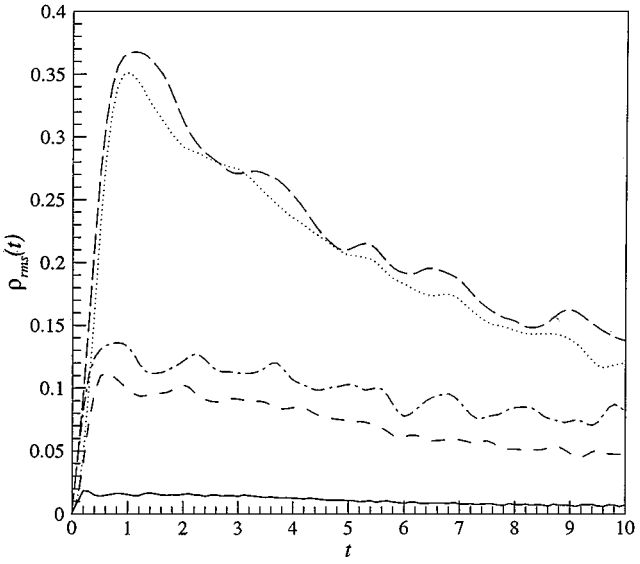

FIG. 18. Time history of ρ_{rms} for the ENO scheme (128^3 grid). Case 1 ———; Case 2 -----; Case 3 -·-·-·-; Case 4 · · ·; Case 5 – – – – –.

3. EVALUATION OF THE BUILT-IN DISSIPATION

3.1. *Measurement of the Numerical Diffusion*

In the previous section, we showed that the nature of the schemes and their respective accuracies deeply affect the solutions. In particular, we recall that the Jameson scheme

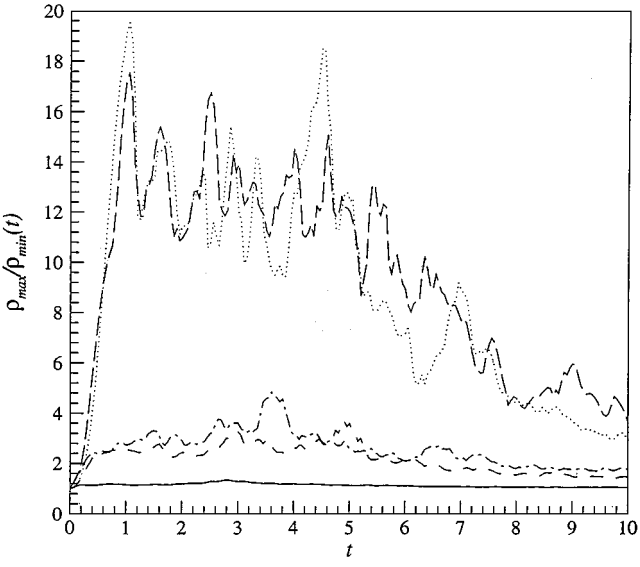

FIG. 19. Time history of density contrast for the ENO scheme (128^3 grid). Case 1 ———; Case 2 -----; Case 3 -·-·-·-; Case 4 · · ·; Case 5 – – – – –.

(with the standard coefficients) yields low-Reynolds-number-type behaviour, whereas the dissipation of the others (except MUSCL1) rather acts as a SGS model. To be more precise, a measurement of the numerical diffusion has to be defined.

One way to measure the numerical diffusion is to compare the MILES results with theoretical results or with results from direct numerical simulation, as it was done by Mossi [8] for the Taylor–Green vortex-decay problem.

In [8], the dynamics of the viscous Taylor–Green flow was investigated with the Jameson and the MUSCL4 schemes on 64^3 and 128^3 grid point meshes without any molecular or SGS diffusion. The results were then compared with the viscous ones obtained by Brachet *et al.* [9] who used a full spectral DNS on a 256^3 grid. The inviscid MUSCL4 results on the 128^3 grid and those computed with the Jameson scheme on the 64^3 grid are in good agreement with those by Brachet *et al.* at respectively $Re = 800$ and $Re = 200$. The numerical diffusion is then easily quantified in terms of an effective Reynolds number equivalent to the diffusion of the scheme.

In the same way, the comparison of velocity-gradients pdfs done in the previous section can give, via a Reynolds number Re_λ based on the Taylor micro-scale, an estimate of the importance of the numerical diffusion.

These methods provide only a global value of the numerical diffusion. However, to compare the numerical diffusion with the SGS one, a local measurement of the former is needed. The numerical diffusion ε_{num}, which is strongly linked to the leading terms of the truncation errors, is interpreted as the difference between the convection terms in momentum equation given by the shock-capturing (*sc*) schemes and the ones given by a reference (*ref*) centered scheme on the same flow field. These two terms are generated by taking a norm of the respectively discretized convective fluxes $\mathcal{F}_{ij}^{sc}$ and $\mathcal{F}_{ij}^{ref}$ where, in the continuous case, they are expressed as

$$\mathcal{F}_{ij} = \rho u_i u_j + \delta_{ij} p.$$

The centered reference flux $\mathcal{F}_{ij}^{ref}$ is chosen in such a way that $(\mathcal{F}_{ij}^{ref}|_{l+1/2} - \mathcal{F}_{ij}^{ref}|_{l-1/2})/\Delta$ is one order more accurate than $(\mathcal{F}_{ij}^{sc}|_{l+1/2} - \mathcal{F}_{ij}^{sc}|_{l-1/2})/\Delta$, where $\mathcal{F}_{ij}^{ref}|_{l+1/2}$ and $\mathcal{F}_{ij}^{sc}|_{l+1/2}$ denote the fluxes evaluated at the right interface of the l cell. Giving ε_{num} the form of an energy dissipation rate, we define

$$\varepsilon_{\text{num}} = \left\langle u_i \frac{\partial}{\partial x_j} \left(\mathcal{F}_{ij}^{sc} - \mathcal{F}_{ij}^{ref} \right) \right\rangle, \tag{9}$$

where the Einstein summation convention applies to repeated indices as in the sequel of this paper. In the finite volume approach, the application of the Gauss theorem allows us to compute directly the divergence of the convective fluxes. Therefore, Eq. (9) becomes

$$\varepsilon_{\text{num}} = \left\langle \frac{1}{V} u_i \left(Q_i^{sc} - Q_i^{ref} \right) \right\rangle, \tag{10}$$

where $Q_i^{sc} = V(\partial/\partial x_j)\mathcal{F}_{ij}^{sc}$ and V is the cell volume; for example, Q_i^{sc} is given by Eqs. (22) and (23) for the MUSCL scheme. For the Jameson scheme, the difference of the two convective fluxes is reduced to the artificial dissipation **D**, as described in Eq. (19), namely

$$\varepsilon_{\text{num}} = \left\langle \frac{1}{V} u_i D_i \right\rangle. \tag{11}$$

TABLE IV
Re_λ Values at $t = 10$ for Case 1

	ENO	WENO	MENO	Jameson	MUSCL4
64^3	27.4	30.6	33.5	30.9	31.6
128^3	35.7	41.3	46.1	37.0	40.2

Now that a measure of the numerical diffusion is defined, it is possible to build an equivalent Reynolds number based upon the pseudo Taylor micro-scale λ introduced in Subsection 2.1,

$$Re_\lambda = \frac{15\langle\rho\rangle(2/3\ \mathbf{E})^{3/2}}{\varepsilon_{\text{num}}\lambda}. \tag{12}$$

The values of Re_λ for Case 1 are summarized in Table IV for both grids at $t = 10$.

As expected, Re_λ increases with the resolution. As we already mentioned when looking at the velocity derivatives pdfs, the Re_λ was estimated to be about 25. It is then remarkable that this estimate is of the same order as the one computed with our measurement of numerical diffusion.

3.2. *Spectral Distribution of the Numerical Errors*

The numerical dissipation ε_{num} measures a norm of the numerical error, but it does not provide any information about the spectral distribution of this error. To get this information, the modulus of the transfer function $\mathcal{T}_m(k)$ for the convective fluxes F_m, G_m, and H_m is computed for each shock-capturing scheme as

$$\mathcal{T}_m(k) = \frac{(1/2)\sum_{k-1/2<|\mathbf{k}|\le k+1/2}\left|\text{FFT}\left(\partial F_m^{sc}/\partial x + \partial G_m^{sc}/\partial y + \partial H_m^{sc}/\partial z\right)\right|^2}{(1/2)\sum_{k-1/2<|\mathbf{k}|\le k+1/2}|ik_1\,\text{FFT}(F_m) + ik_2\,\text{FFT}(G_m) + ik_3\,\text{FFT}(H_m)|^2}, \tag{13}$$

where $\text{FFT}(\cdot)$ denotes the fast Fourier transform and $1 \le m \le 5$. The *transfer function* $\mathcal{T}_m(k)$ corresponds to the ratio between the Fourier transform of the divergence of the convective fluxes computed with the shock-capturing schemes F_m^{sc}, G_m^{sc}, and H_m^{sc}, and the Fourier spectral divergence of the fluxes constructed with the state vector $\mathbf{U}$, as defined in Eq. (2). The modulus of the transfer function is computed here instead of the usual transfer function because our interest focuses only on the dissipative behaviour of the schemes and not on the dispersive errors.

The modulus of the transfer function $\mathcal{T}_2(k)$, corresponding to the component $U_2 = \rho u$, is given in Fig. 20 for the Case 1 on the 128^3 grid at $t = 10$. Results for $\mathcal{T}_3(k)$ and $\mathcal{T}_4(k)$ (not shown here) are very close to the previous ones because of the isotropy of the flow. Obviously, numerical damping leads to a decrease of $\mathcal{T}_m(k)$. Cut-off wave numbers, defined here as the smallest wave number for which $\mathcal{T}_m(k) \le 0.9$, could be deduced from Fig. 20. These wave numbers are evaluated to be about 27 for the MENO and WENO schemes, 18 for the ENO and MUSCL4 schemes, and 14 for the Jameson one. Unfortunately, for $\mathcal{T}_1(k)$, cut-off wave numbers are found at lower values than for $\mathcal{T}_2(k)$, as shown in Fig. 21. The cut-off wave number of the MENO scheme remains around 27, but the one of the Jameson scheme decreases to about 7. This demonstrates that a unique cut-off wave number cannot be defined for a given shock-capturing scheme when dealing with a non-linear system of conservation

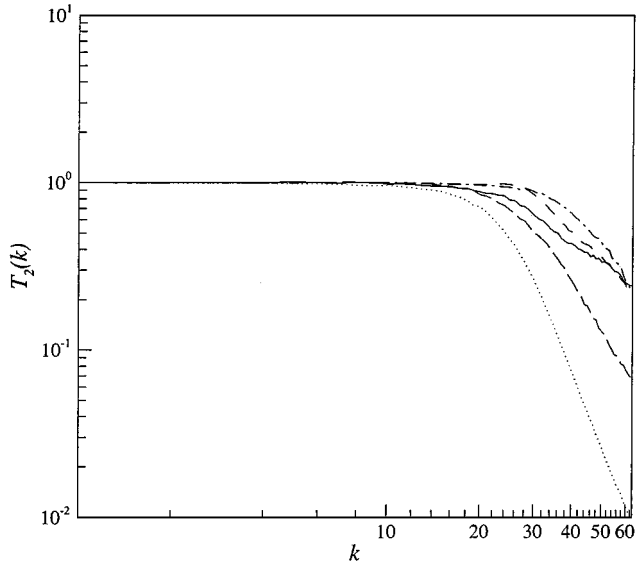

FIG. 20. Transfer function $\mathcal{T}_2(k)$ (Case 1, 128^3 grid, $t = 10$). ENO ———; WENO -----; MENO -·-·-·-·-; Jameson · · ·; MUSCL4 – – – – –.

laws. As a consequence it is impossible to define a unique filter length for a MILES computation on the contrary of a classical LES, which does not satisfy the condition (C2). Moreover, the decay slopes of $\mathcal{T}_1(k)$ are much larger than the ones of $\mathcal{T}_2(k)$, whatever the scheme. Next, one notices the surprising behaviour of the WENO scheme which exhibits for $\mathcal{T}_1(k)$ values slightly larger than one between wave numbers 11 and 21. Finally, for all schemes it is observed that the evolution of $\mathcal{T}_5(k)$ (not shown here) is close to the one of $\mathcal{T}_1(k)$.

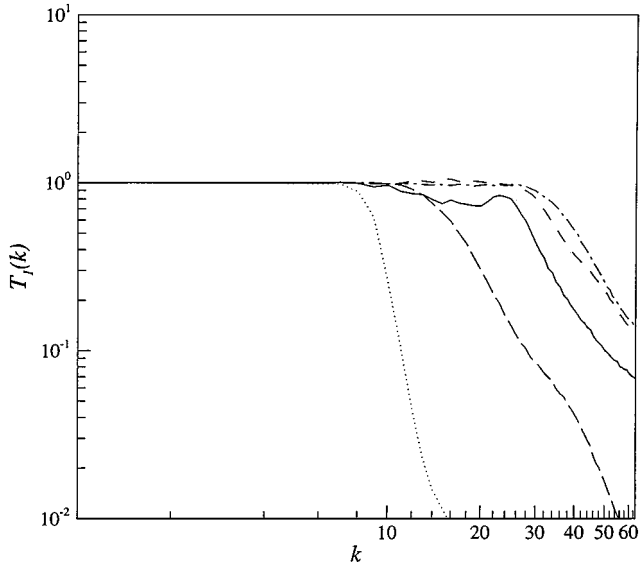

FIG. 21. Transfer function $\mathcal{T}_1(k)$ (Case 1, 128^3 grid, $t = 10$). ENO ———; WENO -----; MENO -·-·-·-·-; Jameson · · ·; MUSCL4 – – – – –.

From this spectral analysis, the ranking between the schemes is consistent with the results previously observed in the kinetic energy spectra (Fig. 6) except for the ENO scheme which exhibits better results than the MUSCL4 scheme. However, despite the same order of accuracy of both schemes, this contrast may be explained by the inconvenient use of the slope limiter by the MUSCL4 scheme, even at low local Mach number.

For all schemes, we observe that the modulus of the transfer functions is smaller than one-third for high wave numbers, leading to a non-physical behaviour of these modes.

3.3. *Generalized Smagorinsky Constant*

From a LES point of view, the numerical diffusion is supposed to be quantified with respect to the SGS one. In this way, the concept of a "generalized Smagorinsky constant" is introduced. The subgrid energy dissipation rate is defined as

$$\varepsilon_{\text{sgs}} = \langle \rho u_i \partial_j \tau_{ij}(\mathbf{u}) \rangle, \tag{14}$$

where τ_{ij} is the subgrid-scale stress tensor expressed in Eq. (40). Here, it is evaluated by means of the Smagorinsky eddy-viscosity model [26] deprived of its constant,

$$\tau_{ij}(\mathbf{u}) = \nu_{\text{sgs}} S_{ij}(\mathbf{u}), \tag{15}$$

with

$$\nu_{\text{sgs}} = \Delta^2 |S(\mathbf{u})| \qquad \text{and} \qquad |S(\mathbf{u})|^2 = 2 S_{ij}(\mathbf{u}) S_{ij}(\mathbf{u}), \tag{16}$$

where $S_{ij}(\mathbf{u}) = \frac{1}{2}(\partial_j u_i + \partial_i u_j)$ and, following Deardorff [27], Δ is related to the mesh size. The strain rate tensor $S_{ij}(\mathbf{u})$ is discretized by means of a second-order centered approximation, which is quite acceptable in the absence of sharp gradients (from now on, only Case 1 is considered).

The "generalized Smagorinsky constant" (hereafter called C_{gs}) is defined as

$$C_{gs} = \sqrt{\varepsilon_{\text{num}}/\varepsilon_{\text{sgs}}}. \tag{17}$$

It corresponds to the value that would take the Smagorinsky constant if the role of SGS diffusion were played by the numerical damping. For example, a value of C_{gs} equal to the classical Smagorinsky constant (C_s) means that the numerical diffusion of the scheme has the same intensity as that of the Smagorinsky SGS model. Note that the theoretical value of C_s for freely decaying turbulence is 0.18 [28], but Deardorff [29] proposed to use 0.2. In Figs. 22 and 23, the time evolution of C_{gs} is given for Case 1. First, a transient phase can be distinguished associated to a fast increase of C_{gs}. This growth of the numerical dissipation is induced by the filling of high frequency modes due to the non-linear energy cascade process. Both ε_{num} and ε_{sgs} follow an enstrophy-like evolution. But at the initial time, ε_{num} is clearly weaker than ε_{sgs} because the flow only contains large structures which are not effected by the numerical damping whereas the existing gradients impose a non-zero SGS dissipation. Up to about $t = 2$, C_{gs} increases quickly (with the filling of the energy spectrum) and later, the ratio $\varepsilon_{\text{num}}/\varepsilon_{\text{sgs}}$ takes a smaller slope. The asymptotic state corresponds to a situation where the decay rate of ε_{sgs} is faster than the one of ε_{num}. The expected self-similar regime is therefore never really reached with the schemes under investigation. Nevertheless, this does not affect the relevance of C_{gs}, which remains much larger than C_s. Therefore we

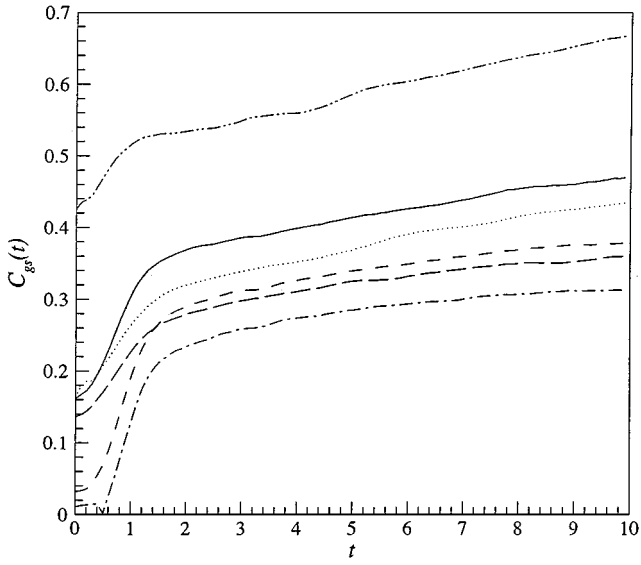

FIG. 22. Time history of C_{gs} (Case 1, 64^3 grid). ENO ———; WENO -----; MENO -·-·-·-·-; Jameson · · ·; MUSCL4 – – – – –; MUSCL1 ·····.

can conclude that all schemes considered overdissipate with respect to the Smagorinsky model, with a ratio between 2.5 and 9 times, depending on the schemes. This does not seem to depend much on resolution. More precisely, C_{gs} is slightly larger with the 128^3 grid than with the 64^3 one. Moreover, the value of C_s is reached a long time before the enstrophy peak for all schemes. Nevertheless, one can notice that the fifth-order accurate MENO scheme is the least dissipative scheme tested in this study. It is followed, ordered by increasing dissipation, by the MUSCL4, WENO, Jameson, ENO, and MUSCL1 schemes.

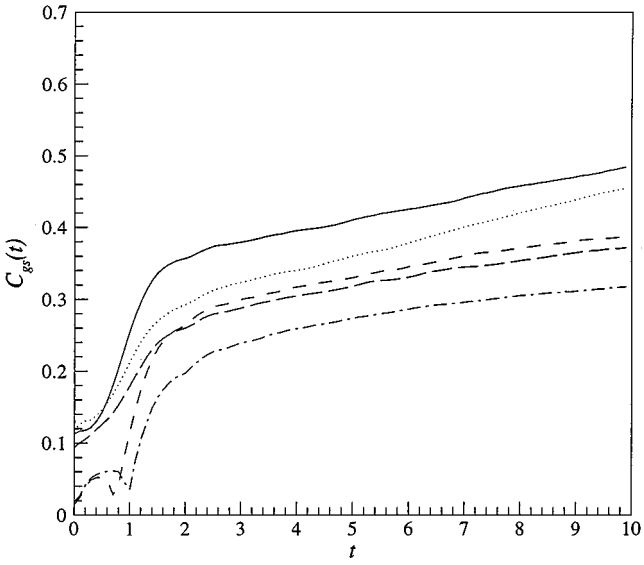

FIG. 23. Time history of C_{gs} (Case 1, 128^3 grid). ENO ———; WENO -----; MENO -·-·-·-·-; Jameson · · ·; MUSCL4 – – – – –.

The third-order MUSCL1 scheme is much more dissipative than the others, as is shown in Fig. 22.

From these results, it appears that the condition (C1) is not fulfilled since $\varepsilon_{\text{num}} > \varepsilon_{\text{sgs}}$. It then can be assumed that the numerical diffusion would mask the effect of the subgrid-scale model in computations where the shock-capturing schemes are coupled with SGS models.

3.4. *Computations with Subgrid Models*

Several computations of the shock-capturing schemes coupled with two different SGS models have been carried out for the shock-free Case 1. The SGS models used in this study are the Smagorinsky and the dynamic eddy-viscosity models, which are both presented in Appendix B.

To compare the MILES concept with classical LES computations, the SGS models are coupled with a fourth-order accurate centered spatial scheme. The spatial scheme is a discretized form of a skew-symmetric formulation of the convection terms, chosen to reduce the aliasing errors, as proven by Blaisdell *et al.* [30]. The three-stage Runge–Kutta TVD scheme is then applied to perform the time integration. This analysis is restricted to Case 1 because SGS models alone are devoid of the shock-capturing ability. The skew-symmetric centered scheme plus the Smagorinsky SGS model is called the S4-SMA scheme and the skew-symmetric centered scheme plus the dynamic eddy-viscosity model is called the S4-DYN scheme.

The kinetic energy spectra of the MENO, S4-SMA, and S4-DYN schemes are represented at $t = 10$ in Fig. 24 for the 64^3 grid. As expected, the S4-SMA scheme (with $C_s = 0.2$) achieves a $-5/3$ slope, whereas the S4-DYN scheme provides a slope slightly smaller than the theoretical one. The square root of the dynamic constant takes the asymptotic value of 0.177 as can be observed in Fig. 25 which shows the time history of $C_d^{1/2}$ on the 64^3 grid. This value is very close to the theoretical value of 0.18. On the contrary, the behaviour for the small scales of the least dissipative shock-capturing scheme tested here (MENO) is far from

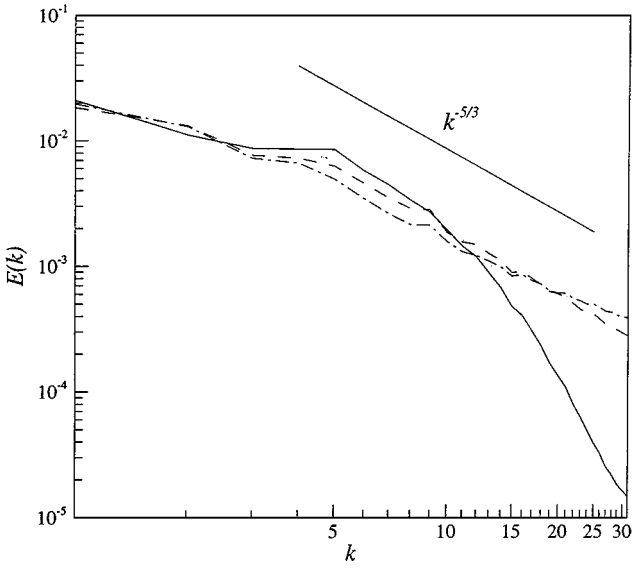

FIG. 24. Kinetic energy spectrum at $t = 10$ (Case 1, 64^3 grid). MENO ———; S4-SMA -----; S4-DYN -·-·-·-·-.

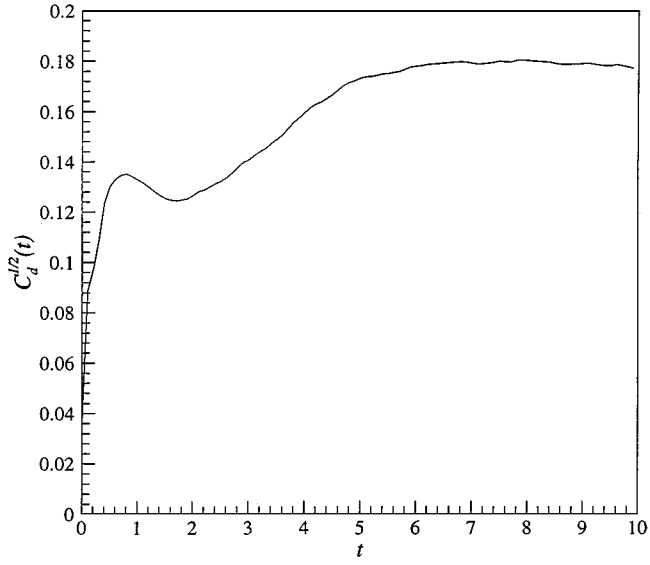

FIG. 25. Time history of square root of the dynamic constant for the S4-DYN scheme (Case 1, 64^3 grid).

being an efficient subgrid model. In the same way, the time history of enstrophy for these three simulations is represented in Fig. 26. The enstrophy level is about one-half times lower for the MENO scheme than for the S4-DYN one. As it appears from Fig. 24, the dynamic eddy-viscosity model is less dissipative than the Smagorinsky at small scales. The Taylor micro-scale values are equal to 3.5 Δ on the 64^3 grid for the schemes S4-SMA and S4-DYN at the end of the simulation. These values can be compared with the value of 4.3 Δ obtained with the MENO scheme on the same grid (see Table II). The conclusion of the comparison between MILES and conventional LES computations is not in favour of the MILES concept.

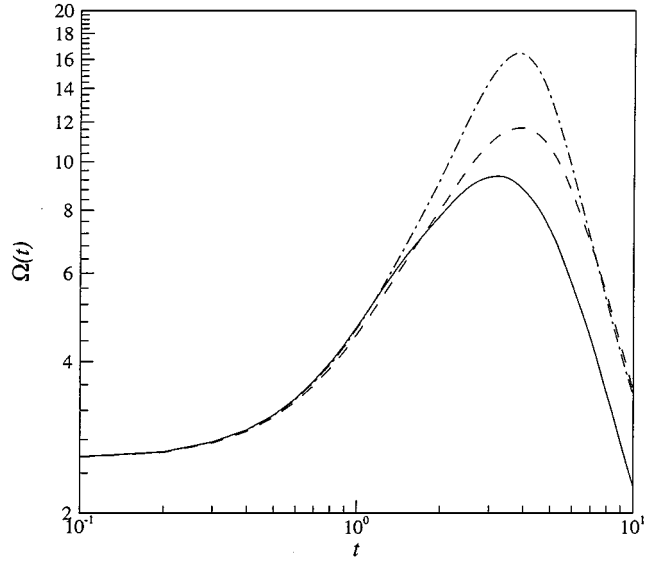

FIG. 26. Time history of enstrophy for the schemes MENO, S4-SMA, S4-DYN (Case 1, 64^3 grid). MENO ———; S4-SMA -----; S4-DYN -·-·-·-.

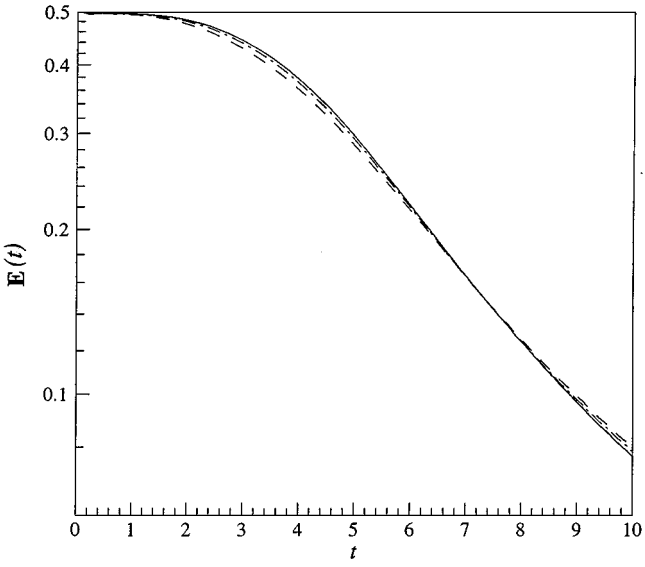

FIG. 27. Time history of energy decay (Case 1, 128^3 grid). MUSCL4 ———; MUSCL4 + Smagorinsky -----; MUSCL4 + dynamic model -·-·-·-·-.

To analyse the effects of a SGS model, the time evolution of the total energy for the MUSCL4 scheme with and without SGS model on the 128^3 grid is shown in Fig. 27. For $t > 7$, the energy level of shock-capturing schemes becomes higher with subgrid model than without. Note that the observations are the same whatever the mesh or the scheme used.

Figure 28 shows the time history of enstrophy on the 128^3 grid for the MUSCL4 scheme with and without models. The subgrid models are seen to add some small scales damping. The kinetic energy spectrum is plotted at $t = 10$ in Fig. 29 for the 128^3 grid. This plot confirms that SGS models provide an additional small scales damping. On the contrary, the

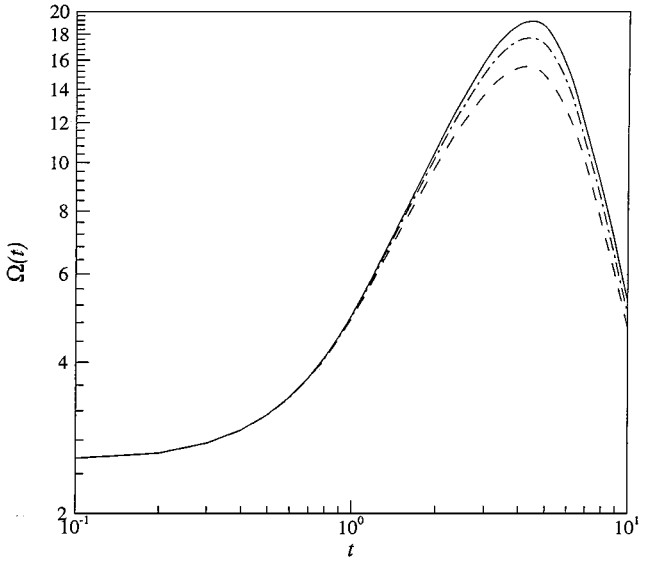

FIG. 28. Time history of enstrophy (Case 1, 128^3 grid). MUSCL4 ———; MUSCL4 + Smagorinsky -----; MUSCL4 + dynamic model -·-·-·-·-.

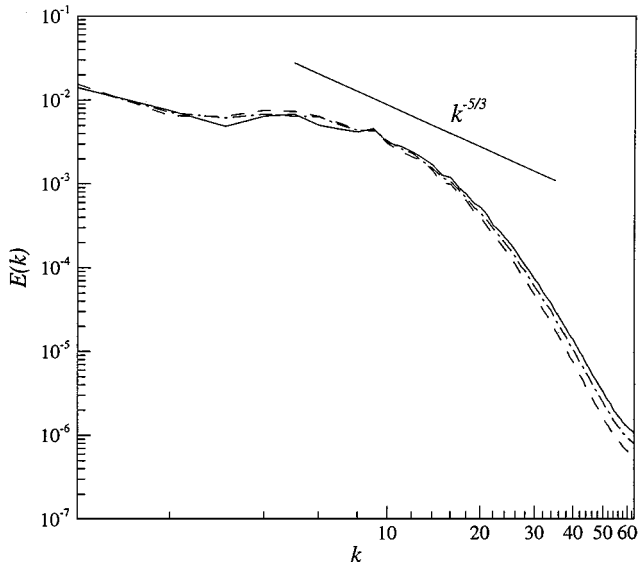

FIG. 29. Kinetic energy spectrum at $t = 10$ (Case 1, 128^3 grid). MUSCL4 ———; MUSCL4 + Smagorinsky -----; MUSCL4 + dynamic model -·-·-·-·-.

large scales become larger with the SGS models than without. Finally, as seen in Fig. 27, the integral of $E(k)$ is larger with a model than without.

In fact, the mechanism is the same as for the Jameson scheme in Euler computation: the additional dissipation provided by the SGS models damps the small scales and prevents the energy transfer from low wave numbers to high ones from occurring. Energy is blocked at small waves numbers where the damping is weak.

The pdfs of $\partial u/\partial y$ at $t = 10$ are plotted in Fig. 30 for the WENO scheme with and without a model on the 128^3 grid. The results are quasi-identical for significant values of

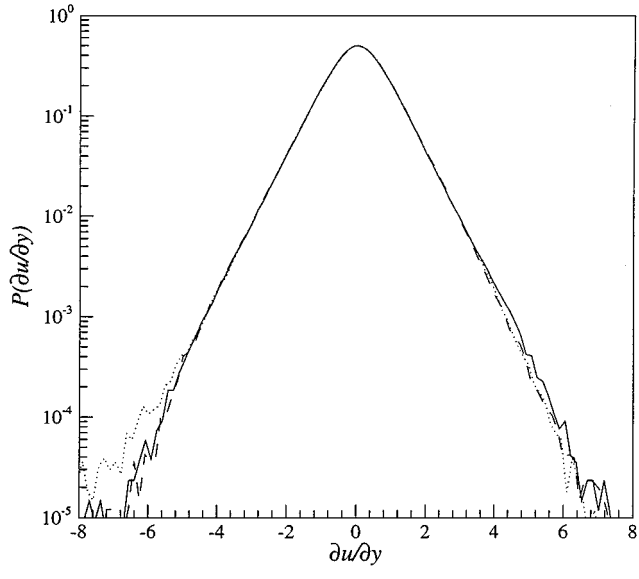

FIG. 30. Probability density function of $\partial u/\partial y$ at $t = 10$ (Case 1, 128^3 grid). WENO ———; WENO + Smagorinsky -----; WENO + dynamic model · · ·.

TABLE V
Taylor Micro-scale Values for All the Schemes with the Smagorinsky and the Dynamic Eddy-Viscosity Models (Case 1, $t = 10$)

ENO + Smagorinsky 7.0 Δ	WENO + Smagorinsky 6.3 Δ	MENO + Smagorinsky 5.5 Δ	Jameson + Smagorinsky 6.5 Δ	MUSCL4 + Smagorinsky 5.9 Δ
ENO + dynamic 6.9 Δ	WENO + dynamic 6.1 Δ	MENO + dynamic 5.3 Δ	Jameson + dynamic 6.4 Δ	MUSCL4 + dynamic 5.7 Δ

the probability. However, for positive values of $\partial u/\partial y$, the wings are slightly smaller with SGS model than without confirming the previous results. The same comments are valid for the other schemes.

The Taylor micro-scale values are given for the 128^3 mesh at $t = 10$ in Table V.

Comparing with Table II, one notices that the Taylor micro-scale increases when SGS models are added to the shock-capturing schemes.

The time history of the C_{gs} is represented in Fig. 31 for the MUSCL4 scheme with and without SGS models (128^3 grid). The values of the C_{gs} are slightly smaller with a model than without. In fact, both overall levels of ε_{num} and ε_{sgs} decrease, but the smoother turbulent field favours the decrease of ε_{num}.

Since the numerical diffusion of the shock-capturing schemes is larger than the diffusion of the SGS models, we can expect the constant C_d of the dynamic eddy-viscosity model to adapt itself to a weak value. The time history of $C_d^{1/2}$ for all the schemes is shown in Fig. 32 on the 64^3 grid. The asymptotic value of $C_d^{1/2}$ is about 0.13 for each scheme used. We observe that the constant decreases from about 0.18 when a centered scheme is used to 0.13 when a shock-capturing scheme is used. This means that the dynamic constant adapts

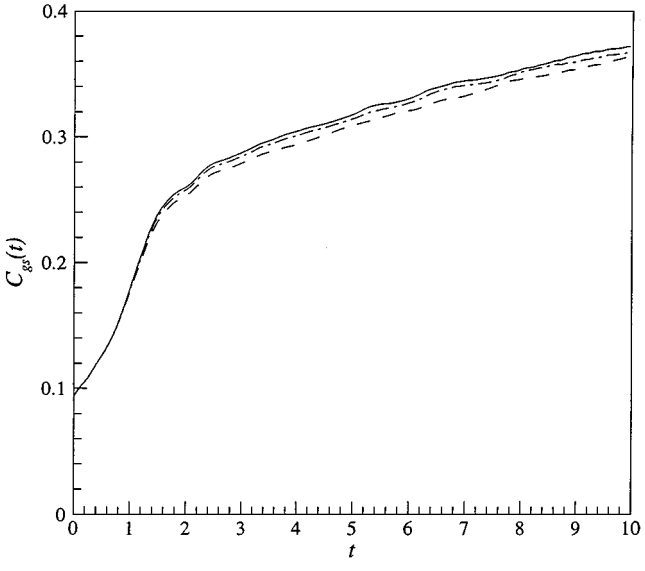

FIG. 31. Time evolution of C_{gs} (Case 1, 128^3 grid). MUSCL4 ———; MUSCL4 + Smagorinsky -----; MUSCL4 + dynamic model -·-·-·-.

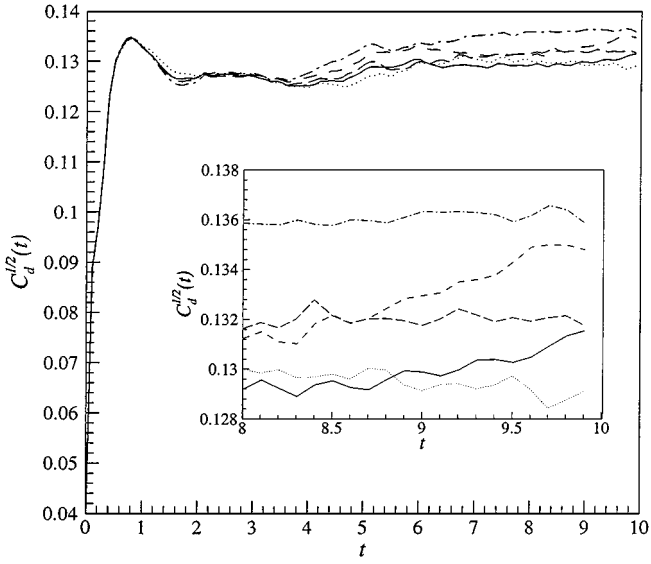

FIG. 32. Time history of $C_d^{1/2}$ when the dynamic model is added to the following shock-capturing schemes (Case 1, 64^3 grid). ENO ———; WENO -----; MENO -·-·-·-·-; Jameson · · ·; MUSCL4 – – – – –.

itself to the dissipation of the schemes, in accordance with the conclusion of Najjar and Tafti [31].

Moreover, since the Jameson scheme prevents the energy to reach the small scales, one could expect the dynamic constant to be very weak. Unfortunately, this constant takes nearly the same value whatever the scheme used. This means that the test filter $\mathcal{G}$ (see Appendix B.2) used here is more sensitive to the large scales than expected. A study about the influence of the test filter upon LES computations can be found in Sagaut and Grohens [32]. A sharper expression of $\mathcal{G}$ gives a lower value of $C_d^{1/2}$ for all schemes but does allow us to differentiate fully the Jameson scheme from the other ones. Nevertheless, one can notice on the enlargement in Fig. 32 that the more diffusive schemes admit a lower value of $C_d^{1/2}$ than the less diffusive ones.

4. CONCLUSION

The intrinsic dissipation of six shock-capturing Euler schemes has been investigated in the case of freely decaying isotropic turbulence simulation with and without SGS models at different rms Mach numbers, compression factors, and resolutions. The general conclusion of this study is that neither the condition (C1) ($\varepsilon_{\text{num}} \ll \varepsilon_{\text{sgs}}$) nor the condition (C2) (ε_{num} mimics ε_{sgs}) is fulfilled by the selected schemes. The MILES approach is able to reproduce few aspects of the fluid turbulence: the worm-like vortices are observed and evidence of $k^{-5/3}$ sub-ranges seems to exist if the resolution is sufficient.

However, a large part of the flow suffers from strong numerical damping. This damping affects every structure defined on less than 5 grid points for all schemes, even in shock-free cases. Moreover, pressure evolution is decorrelated from one of the vortices.

The ENO, WENO, MENO, and MUSCL4 schemes let some energy reach the cut-off wavenumber and preserve the flow from energy accumulation at small scales: in this sense, they behave like a (very dissipative) SGS model. For the Jameson scheme, the influence

of the artificial dissipation is strong: if the set of constants frequently used for industrial transonic computations is retained, a strong damping acting as a cut-off filter appears. Moreover, if a lower artificial dissipation could generate turbulence fields like the other schemes, the same dissipation would probably be insufficient for a LES of a transonic industrial case.

A new measurement of the numerical damping has been introduced in terms of the "generalized Smagorinsky constant" (C_{gs}). This quantity shows that numerical diffusion is considerably larger than the SGS one. The constant C_{gs} can be seen as a new tool to evaluate the numerical schemes in a LES context.

Another important finding is that the addition of a SGS model to the shock-capturing schemes tested in this study is unnecessary and inconvenient. The LES in the transonic regime remains an open problem and improvement of shock-capturing strategies is necessary. Higher-order accurate schemes can be employed, but their computational cost and complexity may prevent their use for industrial applications. Another possibility may be the development of a sensor able to distinguish a turbulent fluctuation from a shock.

A. APPENDIX: SHOCK-CAPTURING SCHEMES

A.1. *Jameson Multi-stage Scheme*

The numerical scheme developed by Jameson *et al.* [33] to solve the Euler equations applies a Runge–Kutta multi-stage (here a four-stage) time integration to the second-order central discretization of the flux balance. Additional dissipation terms are, however, required to capture discontinuities properly and to damp high-frequency oscillations, which are permitted by the scheme.

The Euler equations in conservative form Eq. (1) are here integrated using the finite volume method over a bounded control cell $\Omega_{i,j,k}$ of volume $V_{i,j,k}$ [34]. After the addition of the dissipative terms $\mathbf{D}_{i,j,k}$, the following discretized equation results,

$$\frac{d}{dt}(V_{i,j,k}\mathbf{U}_{i,j,k}) + \mathbf{Q}_{i,j,k} - \mathbf{D}_{i,j,k} = 0, \tag{18}$$

where $\mathbf{U}_{i,j,k}$, attached to the cell center, is an approximation to the average value of $\mathbf{U}$ over $\Omega_{i,j,k}$ and $\mathbf{Q}_{i,j,k}$ is the vector of the net flux leaving and entering $\Omega_{i,j,k}$. The dissipation terms are computed, analogous to the discretization of the convective fluxes, as

$$\mathbf{D}_{i,j,k} = \mathbf{d}_{i+\frac{1}{2},j,k} - \mathbf{d}_{i-\frac{1}{2},j,k} + \mathbf{d}_{i,j+\frac{1}{2},k} - \mathbf{d}_{i,j-\frac{1}{2},k} + \mathbf{d}_{i,j,k+\frac{1}{2}} - \mathbf{d}_{i,j,k-\frac{1}{2}}. \tag{19}$$

The dissipative flux $\mathbf{d}_{i-\frac{1}{2},j,k}$ in I-direction at the cell side $i-\frac{1}{2}, j, k$ is made proportional to the second- and fourth-order differences of the state vector multiplied by a scalar scaling factor r and a weight ε:

$$\begin{aligned}\mathbf{d}_{i-\frac{1}{2},j,k} = {} & r_{i-\frac{1}{2},j,k}\,\varepsilon^{(2)}_{i-\frac{1}{2},j,k}(\mathbf{U}_{i,j,k} - \mathbf{U}_{i-1,j,k}) \\ & - r_{i-\frac{1}{2},j,k}\,\varepsilon^{(4)}_{i-\frac{1}{2},j,k}(\mathbf{U}_{i+1,j,k} - 3\mathbf{U}_{i,j,k} + 3\mathbf{U}_{i-1,j,k} - \mathbf{U}_{i-2,j,k}).\end{aligned} \tag{20}$$

The scaling factor is determined by the spectral radius of the Jacobian matrix for the inviscid flux across the cell face and is formulated according to Jameson *et al.* [33]. The directional

version of the scaling factor proposed by Martinelli [35] has been tested and then abandoned because it was too dissipative; instead, a matrix version as proposed by Swanson and Turkel [36] has been successfully tested in [8] but not included here.

The second- and fourth-order coefficients $\varepsilon^{(2)}$ and $\varepsilon^{(4)}$ are used to adapt locally the dissipative fluxes. They are defined as

$$\varepsilon^{(2)}_{i-\frac{1}{2},j,k} = \kappa^{(2)} \nu_{i-\frac{1}{2},j,k} \qquad \text{and} \qquad \varepsilon^{(4)}_{i-\frac{1}{2},j,k} = \max\bigl(0, \kappa^{(4)} - \varepsilon^{(2)}_{i-\frac{1}{2},j,k}\bigr), \tag{21}$$

where $\kappa^{(2)}$ and $\kappa^{(4)}$ are two constants the typical values of which are between 1.0 and 2.0 for $\kappa^{(2)}$ and between 0.01 and 0.05 for $\kappa^{(4)}$. Here, $\kappa^{(2)}$ has been fixed equal to 1.0 and $\kappa^{(4)}$ equal to 0.03. Simulations with other values have been done but will not be discussed here. We just point out that, in the test Cases 1 and 5, results performed with $\kappa^{(2)} = 1.0$ and $\kappa^{(4)} = 0.01$ are very close to the MUSCL4 ones.

The weight $\nu_{i-1/2,j,k}$, usually referred to as a switch, is formed using the absolute value of the normalized second-order derivative of the pressure field. For the I-direction, this difference can be written as

$$\Psi_{i,j,k} = \left| \frac{p_{i+1,j,k} - 2p_{i,j,k} + p_{i-1,j,k}}{p_{i+1,j,k} + 2p_{i,j,k} + p_{i-1,j,k}} \right|.$$

The switch is then given by

$$\nu_{i-\frac{1}{2},j,k} = \max(\Psi_{i-1,j,k}, \Psi_{i,j,k}).$$

The fourth-order dissipation is automatically switched off in the vicinity of a discontinuity, where the second-order dissipation is large.

A.2. *Roe-TVD Schemes*

A third-order total variation diminishing (TVD) version of the Roe scheme [37, 38] applying the variable extrapolation MUSCL (monotone upstream-centered schemes for conservation laws) approach [39] and a minmod limiter [40] on the characteristic variables is used for the space discretization of the convective terms. The four-stage Runge–Kutta scheme is then applied to the time integration of the resulting system of equations as described in [34].

In the finite volume approximation, the Euler equations (1) are reduced to the simple form

$$\frac{d}{dt}(V_{i,j,k}\mathbf{U}_{i,j,k}) + \mathbf{Q}_{i,j,k} = 0. \tag{22}$$

The net flux $\mathbf{Q}_{i,j,k}$ is written in the same form as Eq. (19), where the Roe flux tensor $\mathbf{q}_{i+1/2,j,k}$ at the interface $i+\frac{1}{2}, j, k$ is expressed as a function of $\mathbf{U}^L_{i+1/2,j,k}$ and $\mathbf{U}^R_{i+1/2,j,k}$, the left and right cell sides extrapolated values of the state vector $\mathbf{U}_{i+1/2,j,k}$. To simplify the notation, the scheme is here described in 1D; the flux tensor $\mathbf{q}_{i+1/2,j,k}$ is therefore replaced by the vector $\mathbf{q}_{i+1/2}$ (the same letter $\mathbf{q}$ is used in both 3D and 1D cases). $\mathbf{q}_{i+1/2}$ is the numerical approximation of the convective flux vector $(\rho, \rho u^2 + p, \rho uh)^t$, h being the total enthalpy defined by $h = \mathcal{E} + p/\rho$. At the interface $i+\frac{1}{2}$, the numerical flux is defined as

$$\mathbf{q}_{i+\frac{1}{2}} = \frac{1}{2}\bigl[\mathbf{q}\bigl(\mathbf{U}^L_{i+\frac{1}{2}}\bigr) + \mathbf{q}\bigl(\mathbf{U}^R_{i+\frac{1}{2}}\bigr)\bigr] - \frac{1}{2}\bigl|\bar{\bar{\mathbf{A}}}\bigl(\mathbf{U}^L_{i+\frac{1}{2}}, \mathbf{U}^R_{i+\frac{1}{2}}\bigr)\bigr|\bigl(\mathbf{U}^L_{i+\frac{1}{2}} - \mathbf{U}^R_{i+\frac{1}{2}}\bigr), \tag{23}$$

where $\bar{\bar{\mathbf{A}}}$ is the Roe matrix constructed from the Roe approximate Riemann solver using the similarity transformation

$$|\bar{\bar{\mathbf{A}}}| = \bar{\bar{\mathbf{T}}}|\bar{\bar{\Lambda}}|\bar{\bar{\mathbf{T}}}^{-1}. \tag{24}$$

$\bar{\bar{\mathbf{T}}}$ and $\bar{\bar{\mathbf{T}}}^{-1}$ are the right and left eigenvector matrices of $\bar{\bar{\mathbf{A}}}$ while $|\bar{\bar{\Lambda}}|$ is the respective diagonal matrix of absolute eigenvalues. The Roe matrix satisfies the following properties:

- $\bar{\bar{\mathbf{A}}}(\mathbf{U}^L_{i+1/2}, \mathbf{U}^R_{i+1/2})[\mathbf{U}^R_{i+1/2} - \mathbf{U}^L_{i+1/2}] = \mathbf{q}(\mathbf{U}^R_{i+1/2}) - \mathbf{q}(\mathbf{U}^L_{i+1/2})$;
- $\bar{\bar{\mathbf{A}}}(\mathbf{U}, \mathbf{U}) = \bar{\bar{\mathbf{A}}}(\mathbf{U}) = \dfrac{\partial \mathbf{q}}{\partial \mathbf{U}}$;
- $\bar{\bar{\mathbf{A}}}$ has real eigenvalues with linearly independent eigenvectors.

The TVD conditions are here achieved by means of the minmod limiter. The left $\mathbf{U}^L_{i+1/2}$ and right $\mathbf{U}^R_{i+1/2}$ state vectors at the cell interfaces are defined as

$$\mathbf{U}^L_{i+\frac{1}{2}} = \mathbf{U}_i + \left[\frac{1+\Phi}{4}\Delta\mathbf{U}^{\lim}_{i+\frac{1}{2}} + \frac{1-\Phi}{4}\Delta\mathbf{U}^{\lim}_{i-\frac{1}{2}}\right] \tag{25}$$

$$\mathbf{U}^R_{i-\frac{1}{2}} = \mathbf{U}_i - \left[\frac{1+\Phi}{4}\Delta\mathbf{U}^{\lim}_{i-\frac{1}{2}} + \frac{1-\Phi}{4}\Delta\mathbf{U}^{\lim}_{i+\frac{1}{2}}\right], \tag{26}$$

where $\Phi = 1/3$ results in a third-order scheme for the scalar convection equation. The limited slopes $\Delta\mathbf{U}^{\lim}_{i-1/2}$ and $\Delta\mathbf{U}^{\lim}_{i+1/2}$ are calculated applying the minmod limiter to the variations of the characteristic variables $\Delta\mathbf{W}$ over the cell interfaces. The $\Delta\mathbf{W}$ are computed from the difference of the primitive variables over a cell side of unit normal surface vector $\mathbf{n}$ as (here in 3D)

$$\begin{aligned}
\Delta W_1 &= \Delta\rho - \frac{1}{c^2}\Delta p \\
\Delta W_2 &= \mathbf{t}_1 \cdot \Delta\mathbf{u} \\
\Delta W_3 &= \mathbf{t}_2 \cdot \Delta\mathbf{u} \\
\Delta W_4 &= \mathbf{n} \cdot \Delta\mathbf{u} + \frac{1}{\rho c}\Delta p \\
\Delta W_5 &= -\mathbf{n} \cdot \Delta\mathbf{u} + \frac{1}{\rho c}\Delta p,
\end{aligned}$$

where $\mathbf{n}$, $\mathbf{t}_1$, and $\mathbf{t}_2$ form an orthonormal basis. The symbol c denotes the speed of sound. In 1D, $\Delta\mathbf{W}$ is reduced to the first, fourth, and fifth components of the 3D vector. The variations $\Delta\mathbf{W}$ are then limited as

$$\Delta\mathbf{W}^{\lim}_{i-\frac{1}{2}} = L(\Delta\mathbf{W}_{i-\frac{1}{2}}, \Delta\mathbf{W}_{i+\frac{1}{2}}) \tag{27}$$

$$\Delta\mathbf{W}^{\lim}_{i+\frac{1}{2}} = L(\Delta\mathbf{W}_{i+\frac{1}{2}}, \Delta\mathbf{W}_{i-\frac{1}{2}}). \tag{28}$$

The minmod [40] version of the limiting function $L(a, b)$ is defined as

$$L^{\text{minmod}}(a, b) = \begin{cases} a & \text{if } |a| < |b| \text{ and } ab > 0 \\ b & \text{if } |a| > |b| \text{ and } ab > 0 \\ 0 & \text{if } ab < 0, \end{cases} \tag{29}$$

where the compression factor β can be set from 1 to 4.

The Roe scheme will be tested here using the lower and the upper compression factor: the former version will be denoted as MUSCL1 and the second one as MUSCL4.

A.3. *ENO, MENO, and WENO Schemes*

Three essentially non-oscillatory (ENO) schemes are considered here. They are all based on the flux reconstruction method described in [13]. In the one-dimensional case, for the scalar conservation law,

$$\frac{\partial u}{\partial t} + \frac{\partial f(u)}{\partial x} = 0, \tag{30}$$

the second-order finite volume discretization of the convective term can be written as

$$\frac{\partial f(u)}{\partial x} = \frac{1}{\Delta x}\left[f\left(x + \frac{\Delta x}{2}\right) - f\left(x - \frac{\Delta x}{2}\right)\right] + O(\Delta x^2), \tag{31}$$

where Δx is the mesh size and $f(x + \frac{\Delta x}{2})$ the classical flux obtained at the cell interface by an arithmetic mean. This discrete approximation is equivalent to the product of convolution of the exact derivation operator with the classical box filter,

$$\frac{1}{\Delta x}\left[f\left(x + \frac{\Delta x}{2}\right) - f\left(x - \frac{\Delta x}{2}\right)\right] \equiv \frac{\partial}{\partial x}\left(\frac{1}{\Delta x}\int_{x-\frac{\Delta x}{2}}^{x+\frac{\Delta x}{2}} f(\xi)\, d\xi\right). \tag{32}$$

The key idea of the ENO schemes is to apply to f a discrete deconvolution operator (denoted A_q) to achieve higher order of accuracy,

$$\frac{\partial f(u)}{\partial x} = \frac{1}{\Delta x}\left[A_q\left(f\left(x + \frac{\Delta x}{2}\right)\right) - A_q\left(f\left(x - \frac{\Delta x}{2}\right)\right)\right] + O(\Delta x^q) \qquad \text{with } q \geq 2. \tag{33}$$

Considering the equivalent differential operator for the box filter, the $(2m+1)$-order inverse operator reads

$$A_{2m+1} = 1 + \sum_{p=1}^{p=m} \Delta x^{2p} a_{2p} \frac{\partial^{2p}}{\partial x^{2p}} + O(\Delta x)^{2m+1}.$$

The coefficients a_{2p} are constant ($a_2 = -1/24$, $a_4 = 7/5760\ldots$). The polynomial A_{2m+1} can be discretized with $r = 2m+1$ points.

As given in [18], the rth-order accurate reconstruction can take the form

$$A_{2m+1}(f_{j+\frac{1}{2}}) = \hat{f}_{j+\frac{1}{2}} = \sum_{l=0}^{r-1} \alpha_{k,l}^r\, f_{j-r+1+k+l} = q_k^r(f_{j+k-r+1}, \ldots, f_{j+k}), \tag{34}$$

where the $\alpha_{k,l}^r$ are the reconstruction coefficients, and k is the stencil index selected among the r candidate stencils. This stencil, called S_k, is defined as

$$S_k = (x_{j+k-r+1}, x_{j+k-r+2}, \ldots, x_{j+k}), \qquad k = 0, \ldots, r-1. \tag{35}$$

To minimize numerical over- and undershoots, the reconstruction is performed with the stencil which provides the most regular solution. Whenever the stencil used to evaluate

$\hat{f}_{i+1/2}$ is different from the stencil used to evaluate $\hat{f}_{i-1/2}$ the order of accuracy decreases to $r-1$. This drawback is limited in the modified ENO (MENO) schemes proposed by Shu [41], which selects automatically the most centered stencil in smooth regions.

Another way to increase the accuracy is the WENO approach [19] which consists in performing linear combinations of the r possible rth-order ENO fluxes. This method increases the theoretical order up to $2r-1$. The WENO fluxes are written

$$\hat{f}_{j+\frac{1}{2}} = \sum_{k=0}^{r-1} \omega_k q_k^r(f_{j+k-r+1}, \ldots, f_{j+k}), \tag{36}$$

where the weights ω_k adapt themselves to the relative smoothness of the flow on each candidate stencil, in such a way that the stencils which contain a discontinuity are assigned a nearly zero weight.

For the Euler equation, the implementation is performed by applying the deconvolution to the characteristic variables. The fluxes at the collocation points are evaluated by means of a Roe solver. Time integration is performed by means of a third-order TVD explicit Runge–Kutta scheme, as recommended in [13].

Using ENO-type schemes, the only source of numerical diffusion is the truncation error which is dependent on the upwinding of the stencils used to compute $\hat{f}_{i+1/2}$ and $\hat{f}_{i-1/2}$. This error denoted as ϵ is analysed on a one-dimensional scalar transport equation. The equivalent partial differential equation associated to a scalar 1D conservation law reads

$$\frac{\partial \phi}{\partial t} + u\frac{\partial \phi}{\partial x} = \epsilon, \tag{37}$$

where ϕ is the advected scalar and u a uniform advective speed. We consider the pair $(k_{\text{left}}, k_{\text{right}})$ for the stencil index used to evaluate $\partial\phi/\partial x$ at the collocation points. The stencil index k_{left} is used to compute $\hat{f}_{i-1/2}$ and k_{right} is used to compute $\hat{f}_{i+1/2}$. In Table VI, the two leading terms of the truncation error and the behaviour induced by this error are provided for $r=3$. In this analysis, u is assumed to be positive.

The notation $\phi^{(i)}$ represents the ith derivative of ϕ with respect to x. The extension of this analysis to complex flows is not straightforward, and the only conclusion is that an anti-diffusive behaviour is *a priori* possible and a dispersive behaviour is often expected. Nevertheless, in the following computations, the mean behaviour is clearly diffusive.

TABLE VI

ENO Scheme Leading Truncation Error Terms for $r=3$

$(k_{\text{left}}, k_{\text{right}})$	ϵ: truncation error	Behaviour of the scheme
(0, 0)	$1/4\Delta x^3\phi^{(4)}$	Anti-diffusive
(0, 1)	$1/3\Delta x^2\phi^{(3)} - 1/4\Delta x^3\phi^{(4)}$	Dispersive + diffusive
(0, 2)	$1/6\Delta x^2\phi^{(3)} - 1/6\Delta x^3\phi^{(4)}$	Dispersive + diffusive
(1, 0)	$-1/3\Delta x^2\phi^{(3)} + 5/12\Delta x^3\phi^{(4)}$	Dispersive + anti-diffusive
(1, 1)	$-1/12\Delta x^3\phi^{(4)}$	Diffusive
(1, 2)	$-1/6\Delta x^2\phi^{(3)}$	Dispersive
(2, 0)	$-1/6\Delta x^2\phi^{(3)} + 1/2\Delta x^3\phi^{(4)}$	Dispersive + anti-diffusive
(2, 1)	$1/6\Delta x^2\phi^{(3)}$	Dispersive
(2, 2)	$1/12\Delta x^3\phi^{(4)}$	Anti-diffusive

B. APPENDIX: SUBGRID SCALE MODELS

The filtered Euler equations, expressed as a function of the filtered variables $\bar{\rho}$, $\bar{p}$, $\tilde{\mathbf{u}} = \overline{\rho\mathbf{u}}/\bar{\rho}$, and $\tilde{T}$, are solved in our computations with SGS models,

$$\frac{\partial \mathbf{U}}{\partial t} + \frac{\partial(\mathbf{F}+\mathbf{F}_{\rm sgs})}{\partial x} + \frac{\partial(\mathbf{G}+\mathbf{G}_{\rm sgs})}{\partial y} + \frac{\partial(\mathbf{H}+\mathbf{H}_{\rm sgs})}{\partial z} = \mathbf{K}_{\rm sgs}, \tag{38}$$

where the subgrid fluxes $\mathbf{F}_{\rm sgs}$, $\mathbf{G}_{\rm sgs}$, and $\mathbf{H}_{\rm sgs}$ and the turbulent stress contribution in energy equation $\mathbf{K}_{\rm sgs}$ are defined as

$$\mathbf{F}_{\rm sgs} = \begin{pmatrix} 0 \\ \bar{\rho}\tau_{11} \\ \bar{\rho}\tau_{12} \\ \bar{\rho}\tau_{13} \\ \breve{q}_1 \end{pmatrix}, \quad \mathbf{G}_{\rm sgs} = \begin{pmatrix} 0 \\ \bar{\rho}\tau_{21} \\ \bar{\rho}\tau_{22} \\ \bar{\rho}\tau_{23} \\ \breve{q}_2 \end{pmatrix}, \quad \mathbf{H}_{\rm sgs} = \begin{pmatrix} 0 \\ \bar{\rho}\tau_{31} \\ \bar{\rho}\tau_{32} \\ \bar{\rho}\tau_{33} \\ \breve{q}_3 \end{pmatrix}, \quad \mathbf{K}_{\rm sgs} = \begin{pmatrix} 0 \\ 0 \\ 0 \\ 0 \\ -\tilde{u}_i \partial_j(\bar{\rho}\tau_{ij}) \end{pmatrix}, \tag{39}$$

where $1 \le i, j \le 3$ and the summation convention applies to repeated indices. The symbol τ denotes the turbulent subgrid-scale stress tensor based on the eddy-viscosity $\nu_{\rm sgs}$,

$$\tau_{ij} = \widetilde{u_i u_j} - \tilde{u}_i \tilde{u}_j. \tag{40}$$

In the energy equation, the pressure-velocity and the pressure-dilatation subgrid terms $\partial_j(\overline{pu_j} - \bar{p}\tilde{u}_j)/(\gamma-1)$ and $(\overline{p\partial_j u_j} - \bar{p}\partial_j\tilde{u}_j)$ are here modeled together as a subgrid-scale heat flux $\breve{\mathbf{q}}$ based on a turbulent Prandtl number Pr_t (here fixed to 0.5), as proposed by Vreman in [42],

$$\breve{q}_j(\tilde{T}) = -\frac{\nu_{\rm sgs}}{\mathrm{Pr}_t M_0^2(\gamma-1)}\partial_j\tilde{T}. \tag{41}$$

Two well-known SGS models have been tested here: the Smagorinsky [26] and the dynamic [43] eddy-viscosity models.

B.1. *Smagorinsky SGS Model*

The Smagorinsky eddy-viscosity model [26] formally models only the anisotropic part of the subgrid-scale stress τ_{ij},

$$\bar{\rho}\tau_{ij} - \frac{\delta_{ij}}{3}\bar{\rho}\tau_{kk} \simeq m_{ij} = -2\bar{\rho}\nu_{\rm sgs}\left[S_{ij}(\tilde{\mathbf{u}}) - \frac{1}{3}S_{kk}(\tilde{\mathbf{u}})\delta_{ij}\right], \tag{42}$$

where $S_{ij}(\tilde{\mathbf{u}}) = \frac{1}{2}(\partial_j\tilde{u}_i + \partial_i\tilde{u}_j)$ is the strain rate and the SGS eddy-viscosity $\nu_{\rm sgs}$ is given by

$$\nu_{\rm sgs} = C_s^2\Delta^2|S(\tilde{\mathbf{u}})| \qquad \text{with } |S(\tilde{\mathbf{u}})|^2 = 2S_{ij}(\tilde{\mathbf{u}})S_{ij}(\tilde{\mathbf{u}}). \tag{43}$$

In this work, the Smagorinsky constant C_s has been chosen equal to 0.2 as proposed by Deardorff [29] for isotropic turbulence and the filter width Δ has been taken equal to the cell size.

B.2. *Dynamic Eddy-Viscosity Model*

The dynamic eddy-viscosity model of Germano *et al.* [43] adopts the eddy-viscosity formulation Eq. (43) where the square of the Smagorinsky constant is replaced by the dynamic coefficient C_d,

$$\nu_{\text{sgs}} = C_d \Delta^2 |S(\tilde{\mathbf{u}})|. \tag{44}$$

This coefficient is dynamically adjusted utilizing information already available at the smallest resolved scales. Let $\mathcal{F}$ be the grid-filter corresponding to the filter width Δ, $\mathcal{F}(w) = \bar{w}$, $\mathcal{G}$ a test-filter corresponding to the filter width $2\,\Delta$, $\mathcal{G}(w) = \hat{w}$, and finally $\mathcal{FG}$ the combination of these two filters associated with the filter width $\kappa\Delta$, $\mathcal{FG}(w) = \hat{\bar{w}}$. In this case and for Gaussian filters, the constant κ is equal to $\sqrt{5}$ [44]. Let moreover τ_{ij} and T_{ij} be the subgrid-scale stress tensor respectively on the $\mathcal{F}$-filter level and on the $\mathcal{FG}$-filter level. Then, the Germano identity yields

$$L_{ij} = \widehat{\bar{\rho}} T_{ij} - \widehat{\bar{\rho}\tau_{ij}} = (\bar{\rho}\tilde{u}_i\tilde{u}_j)\hat{} - \widehat{\bar{\rho}}\check{u}_i\check{u}_j, \tag{45}$$

where $\check{u}_i = \widehat{\bar{\rho}\tilde{u}_i}/\widehat{\bar{\rho}}$. The application of this identity to the eddy-viscosity subgrid tensors on the $\mathcal{F}$-filter level m_{ij} and on the $\mathcal{FG}$-filter level M_{ij} gives

$$L_{ij} = -2C_d M_{ij}, \tag{46}$$

where

$$M_{ij} = \widehat{\bar{\rho}}(\kappa\Delta)^2 |S(\check{\mathbf{u}})| S_{ij}(\check{\mathbf{u}}) - [\bar{\rho}\Delta^2 |S(\tilde{\mathbf{u}})| S_{ij}(\tilde{\mathbf{u}})]\hat{}. \tag{47}$$

Following the least-squares approach of Lilly [45], the dynamic constant C_d is extracted from the six independent equations (46) as

$$C_d = -\frac{1}{2}\frac{\langle L_{ij} M_{ij}\rangle}{\langle M_{ij} M_{ij}\rangle}, \tag{48}$$

where the numerator and the denominator are averaged over the three spatial homogeneous directions in order to prevent numerical instabilities. Classically, C_d is set to zero whenever Eq. (48) returns negative values. However, as one could expect, in the 5 cases analysed here C_d is never negative. Finally, the dynamic eddy-viscosity model has been implemented using the grid of cell size Δ as the global $\mathcal{F}$-filter and a coarser grid of cell size $2\,\Delta$ as the $\mathcal{G}$-filter.

In Section 3, the indices on the field variables will be omitted for ease of notation.

ACKNOWLEDGMENTS

The part of work performed at ONERA was financially supported by DGA/SPAé, French Ministry of Defence. The authors acknowledge L. Machiels for helpful discussions and S. Gavrilakis and J. B. Vos for their useful comments on the draft version of the manuscript.

REFERENCES

1. S. Ghosal, An analysis of numerical errors in large-eddy simulations of turbulence, *J. Comput. Phys.* **125**, 187 (1996).
2. A. G. Kravchenko and P. Moin, On the effect of numerical errors in large eddy simulations of turbulent flows, *J. Comput. Phys.* **131**, 310 (1997).
3. B. Vreman, B. Geurts, and H. Kuerten, Discretization error dominance over subgrid terms in large eddy simulation of compressible shear layers in 2D, *Comm. Numer. Methods Eng.* **10**, 785 (1994).
4. T. Kawamura and K. Kuwahara, *Computation of High Reynolds Number Flow around a Circular Cylinder with Surface Roughness*, AIAA 22nd Aerospace Sciences Meeting (1984).
5. D. H. Porter, A. Pouquet, and P. R. Woodward, Kolmogorov-like spectra in decaying three-dimensional supersonic flows, *Phys. Fluids* **6**(6), 2133 (1994).
6. J. P. Boris, F. F. Grinstein, E. S. Oran, and R. L. Kolbe, New insights into large eddy simulation, *Fluid Dynam. Res.* **10**, 199 (1992).
7. C. Fureby, G. Tabor, H. G. Weller, and D. Gosman, A comparative study of subgrid scale models in homogeneous isotropic turbulence, *Phys. Fluids* **9**(5), 1416 (1997).
8. M. Mossi, *Analysis of Accuracy of Second- and Third-Order Shock-Capturing Schemes by Testing the Taylor–Green Vortex-Decay*, IMHEF-EPFL Technical Report T-97-18, 1997 (unpublished).
9. M. E. Brachet, D. I. Meiron, S. A. Orszag, B. G. Nickel, R. H. Morf, and U. Frisch, Small-scale structure of Taylor–Green vortex, *J. Fluid Mech.* **130**, 411 (1983).
10. O. Métais and M. Lesieur, Spectral large-eddy simulation of isotropic and stably stratified turbulence, *J. Fluid Mech.* **239**, 157 (1992).
11. A. Vincent and M. Meneguzzi, The spatial structure and statistical properties of homogeneous turbulence, *J. Fluid Mech.* **225**, 1 (1991).
12. Z.-S. She, Intermittency and non-gaussian statistics in turbulence, *Fluid Dynam. Res.* **8**, 143 (1991).
13. C. W. Shu and S. Osher, Efficient implementation of essentially non-oscillatory shock-capturing schemes, II, *J. Comput. Phys.* **83**, 32 (1989).
14. T. Passot and A. Pouquet, Numerical simulation of compressible homogeneous flows in the turbulent regime, *J. Fluid Mech.* **181**, 441 (1987).
15. G. A. Blaisdell, N. N. Mansour, and W. C. Reynolds, Compressibility effects on the growth and structure of homogeneous turbulent shear flow, *J. Fluid Mech.* **256**, 443 (1993).
16. G. Erlebacher, M. Y. Hussaini, C. G. Speziale, and T. A. Zang, Toward the large-eddy simulation of compressible flows, *J. Fluid Mech.* **238**, 155 (1992).
17. M. Lesieur, *Turbulence in Fluids* (Kluwer Academic, Dordrecht, 1990).
18. G.-S. Jiang and C. W. Shu, Efficient implementation of weighted ENO schemes, *J. Comput. Phys.* **126**, 202 (1996).
19. X. D. Liu, S. Osher, and T. Chan, Weighted essentially non-oscillatory schemes, *J. Comput. Phys.* **115**, 200 (1994).
20. J. Jiménez, A. A. Wray, Ph. G. Saffman, and R. S. Rogallo, The structure of intense vorticity in isotropic turbulence, *J. Fluid Mech.* **255**, 65 (1993).
21. J. O. Hinze, *Turbulence* (McGraw–Hill, New York, 1975).
22. D. H. Porter, A. Pouquet, and P. R. Woodward, Three-dimensional supersonic homogeneous turbulence: A numerical study, *Phys. Rev. Lett.* **68**(21), 3156 (1992).
23. G. K. Batchelor and Townsend, *Proc. R. Soc. London A* **199**, 238 (1949).
24. A. W. Vreman, B. J. Geurts, J. G. M. Kuerten, and P. J. Zandbergen, A finite volume approach to large eddy simulation of compressible, homogeneous, isotropic, decaying turbulence, *Int. J. Numer. Methods Fluids* **15**, 799 (1992).
25. T. A. Zang, R. B. Dahlburg, and J. P. Dahlburg, Direct and large-eddy simulation of three-dimensional compressible Navier–Stokes turbulence, *Phys. Fluids A* **4**(1), 127 (1992).
26. J. Smagorinsky, General circulation experiments with the primitive equations. I. The basic experiment, *Month. Wealth. Rev.* **91**(3), 99 (1963).

27. J. W. Deardorff, A numerical study of three-dimensional turbulent channel flow at large Reynolds numbers, *J. Fluid. Mech.* **41**, 453 (1970).
28. D. K. Lilly, The representation of small-scale turbulence in numerical simulation experiments, in *Proc. IBM Sci. Comp. Symp. on Environmental Sciences, Yorktown Heights, NY, November 14–16 1967.*
29. J. W. Deardorff, On the magnitude of the subgrid scale eddy viscosity coefficient, *J. Comput. Phys.* **7**, 120 (1971).
30. G. A. Blaisdell, E. T. Spylopoulos, and J. H. Qin, The effect of the formulation of nonlinear terms on aliasing errors in spectral methods, *Appl. Numer. Math.* **21**, 207 (1996).
31. F. M. Najjar and D. K. Tafti, Study of discrete test filters and finite difference approximations for the dynamic subgrid-scale stress model, *Phys. Fluids* **8**(4), 1076 (1996).
32. P. Sagaut and R. Grohens, Discrete filters for large-eddy simulation, *Int. J. Numer. Methods Fluids*, in press.
33. A. Jameson, W. Schmidt, and E. Turkel, *Numerical Simulation of the Euler Equations by Finite Volume Methods Using Runge–Kutta Time Stepping Schemes*, AIAA Paper 81-1259, AIAA 5th Computations Fluid Dynamics Conference (1981).
34. J. B. Vos, P. Leyland, P. A. Lindberg, V. van Kemenade, C. Gacherieu, N. Duquesne, P. Lotstedt, C. Weber, and A. Ytterstrom, *NSMB Handbook 4.0*, EPFL-DGM-IMHEF, 1997 (unpublished).
35. L. Martinelli, *Calculations of Viscous Flows with a Multigrid Method*, Ph.D. Thesis, Department of Mechanical and Aerospace Engineering, Princeton University, 1987 (unpublished).
36. R. C. Swanson and E. Turkel, On central-difference and upwind schemes, *J. Comput. Phys.* **101**, 292 (1992).
37. P. L. Roe, Approximate Riemann solvers, parameter vectors, and difference schemes, *J. Comput. Phys.* **43**, 357 (1981).
38. P. L. Roe, Characteristic based schemes for the Euler equations, *Ann. Rev. Fluid Mech.* **18**, 337 (1986).
39. B. Van Leer, Towards the ultimate conservative difference scheme. V. A second-order sequel to Godunov's method, *J. Comput. Phys.* **32**, 101 (1979).
40. H. C. Yee, Construction of explicit and implicit symmetric TVD schemes and their applications, *J. Comput. Phys.* **68**, 151 (1987).
41. C. W. Shu, Numerical experiments on the accuracy of ENO and Modified ENO schemes, *J. Sci. Comput.* **5**(2), 127 (1990).
42. A. W. Vreman, *Direct and Large-Eddy Simulation of the Compressible Turbulent Mixing Layer*, Ph.D. Thesis, Department of Applied Mathematics, University of Twente, 1995 (unpublished).
43. M. Germano, U. Piomelli, P. Moin, and W. H. Cabot, A dynamic subgrid-scale eddy viscosity model, *Phys. Fluids A* **3**(7), 1760 (1991).
44. M. Germano, Turbulence: The filtering approach, *J. Fluid Mech.* **238**, 325 (1992).
45. D. K. Lilly, A proposed modification of the Germano subgrid-scale closure method, *Phys. Fluids A* **4**(3), 633 (1992).